Influence of dust on precipitation during landfalling atmospheric rivers in an idealized framework

N. R. Mascioli[1], A. Evan[2], M. Ralph[1]

[1]Center for Western Weather and Water Extremes, Scripps Institution of Oceanography, University of California, San Diego, La Jolla, California
[2]Scripps Institution of Oceanography, University of California, San Diego, La Jolla, California

Key Points:

- Dust increases the percentage of precipitation falling as snow/graupel during landfalling atmospheric rivers
- Increases in dust tend to decrease orographic precipitation upwind of the peak and increase orographic precipitation downwind of the peak
- The sensitivity of precipitation to dust depends on the initial thermodynamic structure of the atmosphere

Corresponding author: Nora R. Mascioli, nmascioli@ucsd.edu

Abstract

Atmospheric rivers can provide as much as 50% of the total annual rainfall to the U.S. West Coast via orographic precipitation. Dust is thought to enhance orographic precipitation via the "seeder-feeder" mechanism, in which ice particles from a high cloud fall through a lower orographic cloud, seeding precipitation in the low cloud. Using the Weather Research and Forecasting model, we vary dust concentrations in simulations of two-dimensional flow over a mountain. This idealized framework allows us to test the sensitivity of the precipitation-dust response to a variety of different dust concentrations and initial conditions. The model is run using an ensemble of 60 radiosondes collected from Bodega Bay, CA in 2017-2018, clustered based on their vertical moisture profile into "deep moist", "shallow moist", and "subsaturated" clusters. The principle impact on precipitation is to increase the ratio of precipitation falling as snow. This produces a "spillover" effect, decreasing precipitation upwind of the peak and increasing precipitation downwind of the peak. The largest impacts on the snow/rain ratio occur at the end of the event, during cold front passage. The ensemble mean does not produce a significant seeder-feeder response, however in individual cases with favorable initial conditions there is a significant increase in precipitation throughout the domain due to dust effects on the seeder-feeder mechanism. These findings afford an opportunity to build a more comprehensive understanding for the conditions under which dust aerosol can have a significant impact on precipitation during atmospheric rivers, with implications for future developments in forecasting.

1 Introduction

The United States West Coast can get as much as 50% of its total annual precipitation from a few large storm systems, known as atmospheric rivers (ARs) (Dettinger et al., 2011). ARs are characterized by long narrow bands of moisture where the vertically integrated water vapor transport (IVT) from the surface to 300hPa is $\geq$ 250 kg m^{-1} s^{-1} (Zhu & Newell, 1998; Ralph et al., 2004; Rutz et al., 2014). ARs are generally associated with a parent extratropical cyclone, with the AR core (region of maximum IVT) roughly aligned with the cold front of the extratropical cyclone. As the AR makes landfall, the typical progression is the passage of the warm front, followed by the AR core which is associated with the most intense precipitation, and then the passage of the cold front. Although IVT values generally drop off after the passage of the cold front, there can still be periods of intense precipitation after the cold front passes. A landfalling AR can produce intense precipitation lasting anywhere from hours to days (Dettinger et al., 2011). The bulk of this precipitation occurs due to orographic processes as the moist air mass of the AR is lifted, first by the coastal range, and then by the Sierras.

Most ARs are beneficial for the U.S. West Coast, increasing the availability of water storage and snowpack, but the most extreme events can lead to hazardous events such as floods and debris flow (Dettinger et al., 2011; Ralph et al., 2006, 2019; Oakley et al., 2017). As such, accurately forecasting the precipitation amount, intensity, and type is critically important for water managers in the region. The CalWater campaign (Cordeira et al., 2017; Ralph et al., 2016) was a multiyear series of field experiments between 2009 and 2018 targeted towards improving our scientific understanding and ability to forecast landfalling ARs. Using a combination of targeted research flights, ship and ground based measurements, the CalWater campaigns provided a wealth of data on the structure and intensity of ARs, as well as providing information on the distribution and type of aerosols, including dust and marine aerosols within the AR (Ault et al., 2011; Creamean et al., 2013).

Dust can influence orographic precipitation via its effect on ice nucleation processes (Ault et al., 2011; Creamean et al., 2013; Vali et al., 2015). In mixed phase clouds, such as those seen in atmospheric rivers, ice primarily forms via heterogenous nucleation in

which cloud water and/or water vapor condenses, deposits, and/or freezes onto an ice nuclei. Dust is one of the most abundant and effective types of ice nuclei (Heintzenberg et al., 1996; DeMott et al., 2003; Atkinson et al., 2013; Hande et al., 2015). Cornwell et al. (2019) analyzed in situ measurements of ice nucleating particles (INPs) at coastal sites in California and found that while sea spray aerosols were more abundant in the ambient air, mineral dust particles were the most abundant in ice crystal residuals, i.e. that far more ice crystals nucleated around dust particles than sea spray aerosols. Ault et al. (2011) compared two ARs that made landfall in California in the winter of 2009. The storms had similar characteristics in terms of orientation and IVT maximum, but the second storm produced 1.4 times the precipitation of the first storm. Measurements collected during the CalWater Early Start observational campaign (Ralph et al., 2016) showed that the second storm contained a high concentration of long range transported dust. The authors found that the droplet size was significantly larger in the second storm, and hypothesized that the enhanced precipitation in the second storm was driven by the elevated dust concentrations. Subsequently, in the CalWater-1 field campaign (Ralph et al., 2016), Creamean et al. (2013) found evidence of dust influencing the "seeder-feeder mechanism", in which ice forms in a mid-level "seeder" cloud, and then falls into and becomes rimed in a lower level "feeder" cloud. These hydrometeors then either precipitate as snow/graupel, or melt into liquid droplets. Because ice crystals grow more quickly than liquid water droplets, it is expected that the seeder-feeder mechanism will produce larger droplet sizes and more intense precipitation. Creamean et al. (2015) found that dust and biological particles both served as INPs in storms that made impacted the northern Sierras in the winters of 2009, 2010, and 2011. Dust and biological INPs were typically found in storms with deep convective cloud systems, and biological INPs were most prominent in warm ARs. Creamean et al. (2016) found a similar relationship in the southern Sierras in the winters of 2011 and 2012. In a study of INPs found in precipitation samples during an AR in March 5-6th, 2016, Martin et al. (2019) found a mixture of biological particles, dust, organic carbon, and marine aerosols acting as INPs. Samples were collected at a coastal site (Bodega Bay, CA) and a site in the coastal mountain range (Cazadero, CA). During this AR, the most abundant INPs were biological particles, with dust as the second most abundant. INP concentrations in the precipitation samples were enhanced in the early stages of the AR and following the passage of the cold front. Levin et al. (2019) demonstrated that in some storms, marine INPs can dominate, allowing ice to form at much warmer temperatures. Further research is needed to develop a comprehensive picture of the climatology of what aerosols are most important for ice formation processes during ARs.

Several studies have attempted to model the effects of dust on precipitation during specific storms. Fan et al. (2014) considered the role of dust and other aerosols during two case studies, February 16 and March 2, 2011. Using the WRF model over northern California, they found that dust significantly increased precipitation by as much as 15% over the Sierras during the February 16th AR, but had a much smaller impact on the March 2nd event. Notably, the February 16th storm had a deep cloud layer, which formed after a shallow cloud merged with an elevated cloud layer on February 15th. The cloud top temperature on the 16th was -36°C. In contrast, the March 2nd event had a shallower cloud layer, with a cloud top temperature of only -20°C. Comparison with surface maps from the Weather Prediction Center (WPC) show that the cold front passed northern California around 00Z on February 16 (Weather Prediction Center, 2019), 12 hours before the start of the simulations, explaining the cooler cloud temperatures for this case. Fan et al. (2017) expanded on this analysis by considering a range of dust concentrations for the two cases.

Here, we build on these previous studies by considering a wide range of atmospheric initial conditions and dust concentrations in a theoretical modeling framework. We quantify the sensitivity of precipitation to changes in dust using idealized 2-dimensional WRF simulations. The remainder of this paper is organized as follows: Section 2 describes the

model and data used. Section 3 presents the modeled precipitation response to changes in dust concentration, and discussion and conclusions are presented in Sections 5 and 6, respectively.

2 Data and Methods

2.1 Observations and reanalysis

We test the sensitivity of orographic precipitation during landfalling ARs to increased dust concentration using the WRF model in an idealized 2-dimensional setup (described in Section 2.3). We force the model at its western boundary with a subset (60) of the 245 radiosondes collected at Bodega Bay, CA (star in Figure 2a), home to one of NOAA's Atmospheric River Observatories, during the 2017-2018 Forecast Informed Reservoir Operations (FIRO) field campaign (Table 1) (Jasperse et al., 2017). Bodega Bay is situated at the mouth of the Russian River watershed, which is fed by the Lake Mendocino Reservoir, and gets 30-50% of its annual rainfall from landfalling atmospheric rivers (Dettinger et al., 2011; Ralph et al., 2013). Radiosondes are collected between mid-January and early April each year. The radiosondes collect data on temperature, relative humidity, and height as well as Global Positioning System (GPS) data which is used to calculate wind speed and direction. During landfalling atmospheric river events, sondes are launched at 3 hour intervals, going up to 1.5 hour intervals during peak IVT conditions. The sondes typically collect data from near the surface (below 20 m) through the stratosphere. Sondes launched at 3 hour intervals typically penetrate well into the stratosphere (upwards of 21 km) before the balloon pops, while sondes launched at 1.5 hour intervals typically retrieve data up to the lower stratosphere (15 km) before being terminated. The high temporal density of observations allows us to evaluate the effects of dust on precipitation during different stages of an atmospheric river. The subset of 60 sondes was chosen to provide a large enough sample size to detect a signal out of the statistical noise, while still being a small enough sample to allow us to run a number of different scenarios without becoming too computationally expensive.

As an example, Figure 1 shows three sondes collected during the early, middle and late stages of the January 8-9, 2017 AR. This storm was a strong (AR4) event (Ralph et al., 2019). The first sonde (Figure 1a) was launched at 00Z on January 8th, 2017. At this time in the storm the IVT over Bodega Bay was 384.0 kg m^{-1} s^{-1}. The sonde is saturated in the lower troposphere, up to 850hPa. There is a pronounced dry layer in the mid-troposphere. Above 400hPa, the sonde remains subsaturated, but with a greater relative humidity, suggesting the possibility of forming ice. The winds at the surface are weak and predominantly southerly, strengthening and transitioning to westerlies aloft. The second sonde (Figure 1b) was launched later the same day at 19:30Z. At this point, the AR core (the region of maximum IVT) was passing over Bodega Bay. The storm has a deep moist layer stretching into the mid-troposphere (500hPa) and a calculated IVT of 1086.9 kg m^{-1} s^{-1}. The wind directions are consistent with Figure 1a, but the wind speeds have increased, particularly in the lower and mid troposphere. The third sonde (Figure 1c) was launched at 06Z on January 9th, after the cold front passed Bodega Bay (Weather Prediction Center, 2019). The IVT in this sonde dropped to 372.2 kg m^{-1} s^{-1}. The atmosphere is saturated or near saturation up to 650 hPa, after which the sonde dries off dramatically. Unlike the earlier sondes, this sonde remains completely dry above 600hPa. The surface winds have shifted to westerly flow and decreased in speed, as expected after the passage of a cold front. As we will show in Section 2.2, this structure is fairly typical of a landfalling AR.

In order to get a broader spatial picture of the development and positioning of the landfalling ARs considered here, we also utilize total column precipitable water from the ERA5 reanalysis dataset (Copernicus Climate Change Service (C3S), 2017) over the same time period covered by the radiosondes. ERA5 data is hourly on a 30 km grid with 137

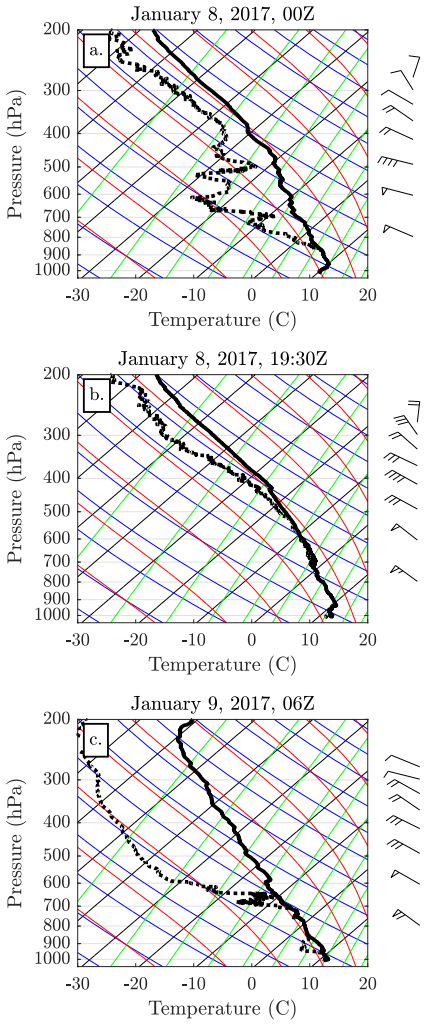

Figure 1. Skew-T log-p for three radiosondes launched from Bodega Bay, CA during the January 8-9, 2017 atmospheric river event. The first sonde (a) was collected early in the event (January 8, 00Z). The second sonde (b) was collected near the peak observed integrated vapor transport (IVT) conditions at Bodega Bay (January 8, 19:30Z). The third sonde (c) was collected shortly after the cold front passed Bodega Bay (January 9, 06Z), as seen in comparisons with surface maps from the Weather Prediction Center (WPC, not shown). IVT is 384.0 kg m^{-1} s^{-1} initially (a), rises to 1086.9 kg m^{-1} s^{-1} (b), and then decreases back to 372.2 kg m^{-1} s^{-1} (c). The thick black lines are the in-situ temperature and the dashed black lines are the in-situ dew point temperature. All other lines and symbols assume their typical definitions.

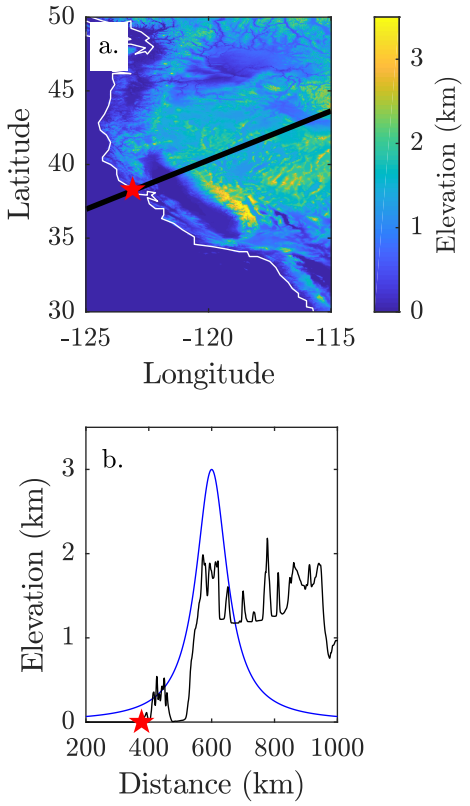

Figure 2. (a) Surface elevation of the Western U.S. The red star signifies the location of the Atmospheric River Observatory (ARO) in Bodega Bay, CA. The dashed line is a sample transect of a typical AR path. (b) Elevation along the transect (black) compared with the idealized model topography (blue), plotted as distance from the model's western boundary.

vertical levels from the surface to 80 km. We also refer to surface maps provided by the National Weather Service Weather Prediction Center for synoptic analysis (Weather Prediction Center, 2019).

2.2 Radiosonde clusters

As discussed previously, Fan et al. 2014 examined the effect of dust on orographic precipitation and found evidence that the thermodynamic structure of the atmospheric river impacts the sensitivity of precipitation to dust. In order to further examine the potential role of the vertical structure of the AR on dust sensitivity, we classify the 245 radiosondes collected at Bodega Bay during the 2017-2018 FIRO field campaigns according to their vertical relative humidity profile using a k-means clustering algorithm. We interpolate the sondes to a common vertical grid with 50 m resolution. For our purposes, we are primarily interested in the moisture profile in the troposphere, so we restrict the clustering algorithm to relative humidity from 50-12500 m. The lowest level of the interpolated sondes (0-50 m) is discarded due to missing data. The algorithm minimizes the euclidean distances between points in the same cluster, and calculates a centroid for each cluster. 20 sondes were removed from the analysis due to missing data. Of the remaining 225 sondes, we find three distinct clusters, shown in Figure 3. We use silhouette analysis (not shown) to determine that the choice of three clusters provides the most

Table 1. FIRO Radiosondes collected at Bodega Bay, CA during Water Years 2017 and 2018.

Month	No. of radiosondes
January 2017	57
February 2017	87
March 2017	16
April 2017	0
January 2018	29
February 2018	0
March 2018	37
April 2018	20

robust separation between clusters. Cluster one (red) consists of 110 "deep moist" sondes. Radiosondes in this group are saturated or near saturated through the mid troposphere (up to 6000 m). Figure 1b is an example of a deep moist sonde. Sondes in the second cluster (76, black) are saturated or near saturated in the lower troposphere (up to 3000 m), and dry aloft (as in Figure 1c). The third and final cluster (blue) is made up of 39 sondes that are subsaturated throughout the troposphere (Figure 1a is an example). However, this cluster was also the most variable, suggesting that to some extent it may represent sondes that don't cleanly fit into the first two clusters. The clusters will be referred to as "deep moist", "shallow moist", and "subsaturated" throughout the text. Figure 4 shows the skew-T log-p of the mean of each of the clusters. While the clusters are generally similar near the surface, on average sondes in the shallow moist cluster are colder in the mid-troposphere (up to 700 hPa) than sondes in the deep moist and subsaturated clusters, which may be evidence of the passage of a cold front.

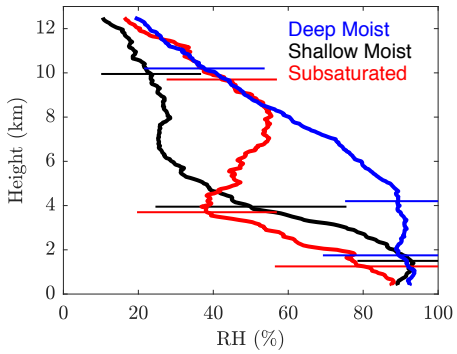

Figure 3. K-means clustering of the vertical moisture profile for radiosondes collected at Bodega Bay during water years 2017 and 2018. We find 3 distinct centroids, which we classify as deep moist (red), shallow moist (black), and subsaturated (blue). Error bars show the standard deviation of relative humidity in the clusters.

To better understand the physical significance of the different clusters, we consider the timing of the radiosonde launches relative to AR landfall. As an example of this, Figure 5 shows total precipitable water (TPW) from ERA5 averaged between -123.5 °E and -122.5 °E during the month of February 2017, with the results of the k-mean clustering of the radiosondes launched during this time overlaid on top. From this we can see that the "deep moist" sondes are generally representative of conditions in the AR core, when

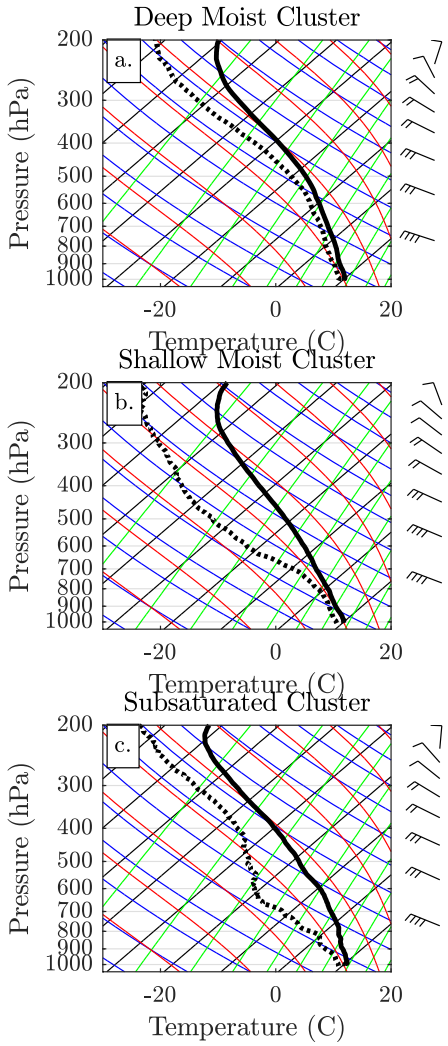

Figure 4. Skew-T of the mean of the (a) deep moist, (b) shallow moist, and (c) subsaturated clusters from Figure 3.

the TPW at Bodega Bay is highest, while the "shallow moist" profiles were typically taken in the late stages of the AR (though a few were also taken in the early stages before the AR made landfall). The subsaturated profiles commonly occur in between the other two states, and may represent a transition between the deep moist and shallow moist sondes, or a lull in AR conditions. This relationship was true over the entire observation period (not shown). Only two events broke this pattern (January 20th, 2017 and March 8, 2018). Both cases featured relatively weak (maximum integrated vapor transport of 474.1 kg m^{-1} s^{-1} and 406.2 kg m^{-1} s^{-1}, respectively) short duration (<24 hrs) events. Comparisons of the timing of the radiosonde launches with the WPC surface archive maps confirms that many of the sondes from the "shallow moist" cluster are associated with the passage of the cold front (Weather Prediction Center, 2019).

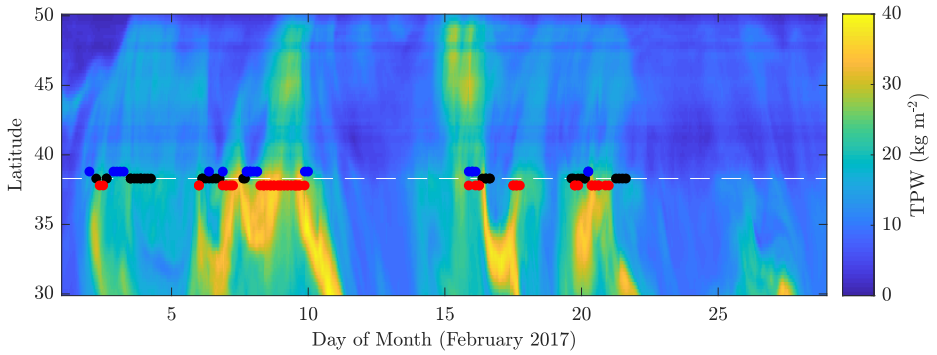

Figure 5. ERA5 total precipitable water averaged from -123.5 °E and -122.5 °E during February 2017. Circles represent the launch time of each radiosonde released from Bodega Bay (38.3N, -123.1E) during February 2017. Deep moist sondes are red, subsaturated sondes are blue, and shallow moist sondes are black.

As part of this analysis, we also considered clusters based around temperature, wind speed, and wind direction. We found that for temperature and wind speed it was not possible to separate the sondes into well-defined clusters. The exception to this was for wind direction. As with relative humidity, we found three clusters related to vertical profiles of wind direction relating to the life cycle of the AR. During the early and mid stages of the AR, winds were typically southerly at the surface and westerly aloft, transitioned to southerly flow at the surface and southwesterly flow aloft, and finally to southwesterly flow throughout the lower and mid troposphere. These clusters produced similar results, in terms of dust impacts on precipitation, to the relative humidity clusters and are not shown. However, as described in Section 2.3 below, wind direction itself is not part of our model setup; in a more realistic framework, clusters based on wind direction may prove to be an important variable for predicting dust impacts on precipitation.

2.3 Model description

In this analysis we use the Advanced Research WRF version 3.9.1.1 (Skamarock et al., 2008) run in an idealized 2-dimensional setup. Our model domain is 1200 km long with a horizontal resolution of 2 km. The model extends to an altitude of 30,000 m with 40 vertical eta levels (terrain following). The horizontal length of the domain is necessary to avoid feedback from the lateral boundaries. A 2 km horizontal resolution allows us to resolve convection, and the model uses a 20 s time step. The lateral boundaries are open boundaries and the top of the model is a periodic boundary.

A bell shaped hill is placed in the center of the domain such that

$$h(x) = \frac{3}{(1 + \frac{x}{0.03})^2} \tag{1}$$

where *h(x)* is the height of the topography in km and x is the lateral distance from the center of the domain (km). Figure 2b compares the model topography with a sample transect of topography along the path of an AR. Note that the height of the inland mountain range in California varies from 2 km to 4 km (Figure 2a), so 3 km serves as an approximation of the mean height of the Sierras. Each simulation is run for 36 hours, with the first 12 hours discarded as spin up.

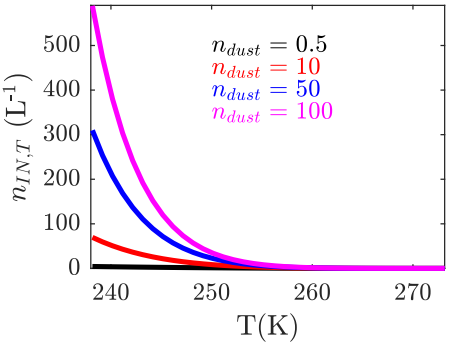

Figure 6. Number of activated ice nuclei using the DeMott et al. (2010) parameterization as a function of temperature for different dust concentrations (in cm^{-3}).

We run WRF using the Thompson Aerosol-Aware microphysics scheme (Thompson & Eidhammer, 2014), a bulk microphysics scheme which explicitly predicts the mass mixing ratios of cloud water, cloud ice, snow, graupel, and rain as well as the number concentrations of cloud water, cloud ice, and rain. The scheme is an adaption of the previous Thompson microphysics scheme (Thompson et al., 2008) that has been modified to include aerosols acting as cloud condensation nuclei (CCN) and ice nucleating particles (INP). The Thompson scheme is commonly used in operational forecast models, and in particular is used in West-WRF, a version of the WRF model which has been optimized for forecasting precipitation in the western U.S. In order to reduce the computational expense, aerosols are classified as hygroscopic (potential CCN) or non-hygroscopic (potential INP). Hygroscopic aerosols are a combination of sulfates, sea salt, and organic matter. For the purposes of this idealized study, non-hygroscopic aerosols are assumed to be dust. Dust activates into cloud ice following the DeMott et al. (2010) ice nucleation parameterization

$$n_{IN,T} = a(273.16 - T)^b (n_{INP})^{(c(273.16-T)+d)} \tag{2}$$

where $n_{IN,T}$ is the number concentration of activated INP at temperature T, T is the in situ temperature (K), n_{INP} is the number concentration of INPs, and a, b, c, and d are empirically determined constants, where $a = 5.94 * 10^{-5}$, $b = 3.33$, $c = 0.0264$, and $d = 0.0033$. For the purposes of this theoretical study, we assume that INPs are dust, i.e. $n_{INP} = n_{dust}$. Figure 6 shows the relationship between $n_{IN,T}$ and T for different INP concentrations. In all cases, $n_{IN,T}$ increases as INP concentration increases and as T decreases. The largest differences between $n_{IN,T}$ from the different INP scenarios occur at colder temperatures. Supercooled water droplets freeze into ice follow-

ing the Bigg (1953) scheme, but with the effective temperature modified by the INP concentration, such that higher concentrations produce more ice (Thompson & Eidhammer, 2014). Aqueous aerosols freeze into ice crystals following Koop et al. (2000). Secondary ice formation from rime splinters occurs following the Hallet-Mossop process (Hallett & Mossop, 1974; Reisner et al., 1998; Thompson et al., 2008).

For the purposes of this experiment, we prescribe background values of CCN to be 300 cm^{-3} (the default concentration in the Thompson scheme). To test the model sensitivity to dust, we consider six different scenarios with dust concentrations of 0.5 cm^{-3}, 2 cm^{-3}, 4 cm^{-3}, 10 cm^{-3}, 50 cm^{-3}, and 100 cm^{-3}. Throughout the text we will refer to these scenarios as INP0.5, INP2, INP4, INP10, INP50, and INP100. INP0.5 approximates a climatological average of dust values (Creamean et al., 2014); INP2 and INP4 represent observed values during the CalWater field campaign (Fan et al., 2014). INP10 represents high dust concentrations within a transported dust layer (Fan et al., 2017), and INP50 and INP100 are included to provide the full shape of the power law relationship between dust and ice formation (Section 3), as well as allowing us to span the ranges of results used elsewhere in the literature (Fan et al., 2017). Dust is assumed to have a constant vertical profile at the start of the simulation. Aerosols are removed when they are activated into CCN and INP. While this does not produce a realistic representation of real world dust profiles, it is useful for testing sensitivity to increased dust concentrations in this idealized framework.

Aside from the Thompson microphysics parameterization, all other parameterization options are set to the default value for WRF. We use the radiosondes collected at Bodega Bay (Section 2.1) to force the model at the western lateral boundary. For each dust scenario, we construct a 60-member ensemble by varying the initial conditions at the western lateral boundary using a randomly selected subset of 20 radiosondes (included as supplemental material) from each of the three clusters described in Section 2.2. As described in Section 2.2, the radiosondes were sorted into three clusters based on their vertical profiles of relative humidity. Each sonde provides data on pressure, temperature, relative humidity, wind speed and wind direction which we use to calculate virtual potential temperature and specific humidity. The variables are then interpolated to 50 m vertical intervals to be input into the idealized WRF model.

3 Dust sensitivity

As detailed in Section 2.3, we examine the effects of dust on orographic precipitation using the WRF model run with an idealized 2-D hill setup. For each dust scenario, we construct an ensemble by forcing the model with 60 of the 245 radiosondes collected at Bodega Bay in 2017-2018. The ensemble mean daily average (hours 12-36 in the simulations) total precipitation (liquid and frozen) in our low dust scenario (INP0.5) maximizes at 90 mm slightly upwind of the peak of the 3000 m hill (Figure 7a). Up to 62% of total precipitation falls as snow upwind of the peak, while as much as 85% falls as snow immediately downwind of the peak. In contrast, the majority of the graupel falls upwind of the peak (up to 21% of total precipitation) while 12% of the precipitation downwind in the lee of the peak falls as graupel.

In order to test the precipitation response to dust, we use the low dust (INP0.5) scenario as our control run and perform a series of sensitivity experiments with increased average dust concentrations (n_{dust}): INP2, INP4, INP10, INP50, and INP100. Increasing dust increases the percentage of total precipitation falling as snow and graupel over the peak at all dust levels (Figure 7). This shift from rain to frozen precipitation causes total precipitation to decrease on the upwind slope of the mountain, and increase on the downwind slope (Figure 7b). This change is primarily due to the increase in the amount of precipitation falling as snow at higher dust concentrations. The net effect on precipitation over the mountain is small, but the increased snow/rain ratio advects precipita-

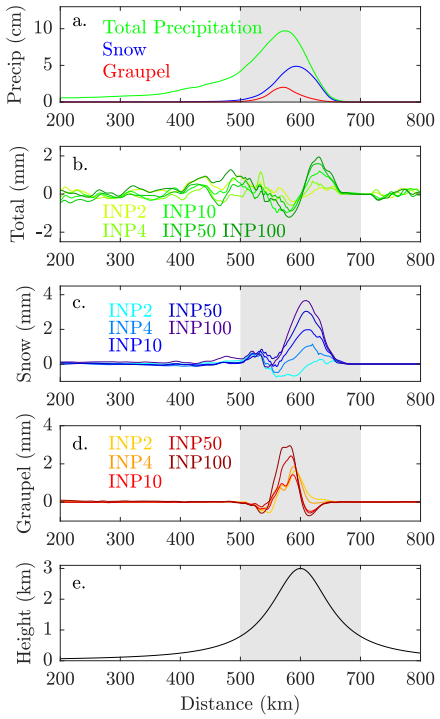

Figure 7. Ensemble mean (60 members) (a) Daily average total precipitation, snow, and graupel in the control scenario (INP0.5) and (b) changes in daily average precipitation, (c) snow, and (d) graupel between the control, and a set of simulations with elevated dust concentrations (INPx-INP0.5). (e) Terrain height is provided for comparison. Grey shaded regions show the location of the mountain.

tion towards the lee side of the mountain. This displacement is sometimes referred to as a "spillover effect", and occurs as a result of the slower fall speed of snow compared to rain (B. Colle & Mass, 2000; B. Colle, 2004; B. A. Colle & Zeng, 2004; B. A. Colle et al., 2005; Morales et al., 2018; Wallmann & Milne, 2007). The increase in the percentage of precipitation falling as snow and graupel is driven by increases in ice water path (IWP), particularly upwind of the peak (Figure 8c). This increase comes at the expense of liquid water path (LWP), which decreases by a similar amount over the same region (Figure 8b). Additionally, the increase in graupel upwind of the peak, on the order of 5% (INP2) to 12% (INP100) averaged from 550 km to 600 km, is evidence that there is an increase in riming processes due to increased dust concentrations. This suggests that in the ensemble mean, dust may be enhancing the seeder-feeder mechanism, but that the overall effect on precipitation is small relative to the orographic forcing of the mountain (on the order of 0.1% for INP2 to 0.4% for INP100 averaged from 550 km to 650 km).

Fan et al. (2014) and Fan et al. (2017) demonstrate that the impacts of dust can vary significantly depending on the characteristics of the storm, and so we sort the simulations based on the clustering of the input sondes described in Section 2.2. By design, the 60 input sondes were randomly selected so that there are 20 sondes from each cluster. Figure 9 shows the daily average total precipitation, snow, and graupel in the control run for each of the 3 clusters. Unsurprisingly, the daily average precipitation, snowfall, and graupel are greatest for the deep moist simulations, and least in the subsaturated case. Comparing the deep moist and shallow moist simulations, the overall precipitation totals are similar, but the percentage of precipitation falling as snow is smaller

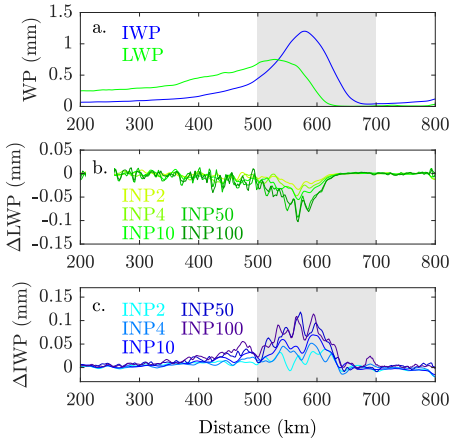

Figure 8. (a) Daily average ensemble mean liquid water path (LWP, green) and ice water path (IWP, blue) in the control scenario. (b) Changes in daily average LWP and (c) IWP between the control, and a set of simulations with elevated dust concentrations (INPx-INP0.5). Grey shaded region shows the location of the mountain.

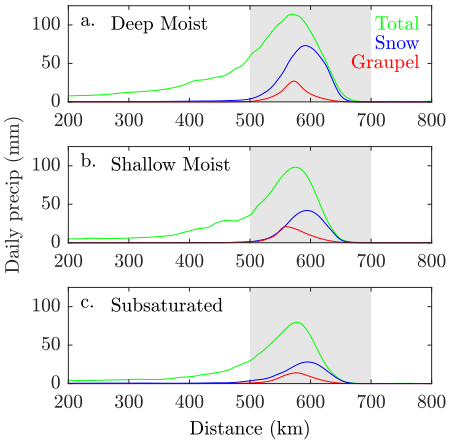

Figure 9. As in Figure 7a, but with the ensemble members split into the (a) deep moist, (b) shallow moist, and (c) subsaturated clusters shown in Figure 3.

in the shallow moist case due to the lower moisture availabilty above the freezing level (Figure 4b). The deep moist cluster has stronger updrafts upwind of the mountain, with a mean vertical velocity of 1.19 m s^{-1} averaged from 550 - 600 km and from the surface to 5 km (Figure 10a). In contrast, the updrafts upwind of the mountain in the shallow moist (mean vertical velocity of 0.77 m s^{-1}, Figure 10b) and subsaturated (mean vertical velocity of 0.66 m s^{-1}, Figure 10c) cases are relatively weak. The cloud layer in the deep moist cluster extends to heights of 12 km, even before being lifted orographically (Figure 11ab). In contrast, the shallow cluster's cloud layer is capped at around 5 km before being lifted (Figure 11e), while the subsaturated cluster has a low cloud (also capped around 5 km), as well as a high ice cloud in the upper troposphere (up to 15 km; Figure 11cd). The shallow cluster is a purely warm cloud until it is orographically lifted and begins to form ice (Figure 11f). As a result of their weaker convection, the shallow moist (Figure 12b) and subsaturated (Figure 12c) clusters have significantly more supercooled

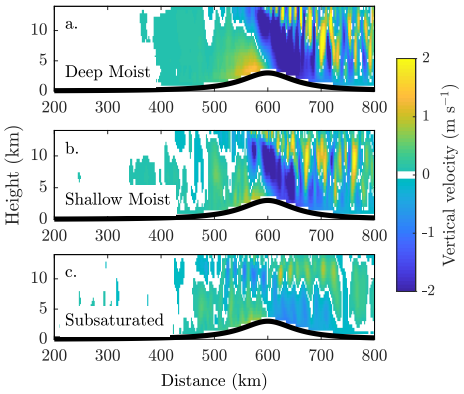

Figure 10. Ensemble average vertical velocities (m/s) in the (a) deep moist, (b) shallow moist, and (c) subsaturated clusters.

water available (0.33 g kg^{-1} and 0.29 g kg^{-1} averaged from 500 - 600 km from the western boundary and from the surface to 5 km) than the deep moist cluster (0.19 g kg^{-1}, Figure 12a), which already has significant ice formation in the low dust simulation.

As seen in the ensemble average (Figure 7bcd), increasing the dust concentration leads to increases in the snowfall over the mountain (Figure 13def), increases in graupel upwind of the peak (Figure 13ghi), and decreases in total precipitation upwind of the peak coupled with increases in total precipitation in the lee of the peak (Figure 13abc) in all clusters. The changes in total precipitation upwind of the peak are small relative to the precipitation in the control (decreases on the order of 1% or less). Downwind of the peak, the increases in total precipitation are on the order of 1% (INP2) to 5% (INP100) in each of the clusters. The total change in precipitation averaged over the peak (550km-650km) is not significantly different from zero for any cluster or INP concentration (Figure 14abc), where significance is determined using a student-T test with 95% confidence.

There are notable differences in the relative and absolute magnitudes of the modeled changes in frozen precipitation. In the subsaturated and deep moist cases, changes in snowfall range from near zero (INP2), to increases of 4 mm (INP50, INP100; Figure 13df). In contrast, in the shallow moist case, there are clear increases in snowfall, especially at lower dust concentrations (2 mm-3 mm at INP2 and INP4, up to 6 mm at IN100; Figure 13e). In relative terms, the changes in snowfall also represent a much larger percentage increase in the shallow moist case: 9% to 25% (INP2 to INP100) over the peak, compared with 6% to 18% in the subsaturated case and 2% to 10% in the deep moist case. Averaged over the peak, we find that the mean changes in snow are significant for all INP concentrations in the shallow cluster (Figure 14e), and for INP4, INP50 and INP100 for the subsaturated cluster (Figure 14f). The deep moist cluster has two outlier cases that were extremely sensitive to increased INPs (not shown for INP100), but the ensemble mean did not differ significantly from zero (Figure 14d).

When considering graupel on the other hand, the shallow moist case shows the smallest changes in both the absolute and relative sense. Averaged over the upwind slope of the peak (550-600 km from the western boundary), graupel increased by 0.16 mm (INP2) to 0.52 mm (INP100), with maximum increases of up to 2.3 mm (Figure 13h). These changes represent 0.5% to 3.0% increases in graupel. The absolute changes in graupel are similar in the subsaturated and deep moist cases for the higher dust concentrations (INP10 through INP100), on the order of 1 mm-2 mm, but at the lower concentrations (INP2 and INP4), the changes in graupel are larger in the deep moist case (0.8 mm-1.0 mm)

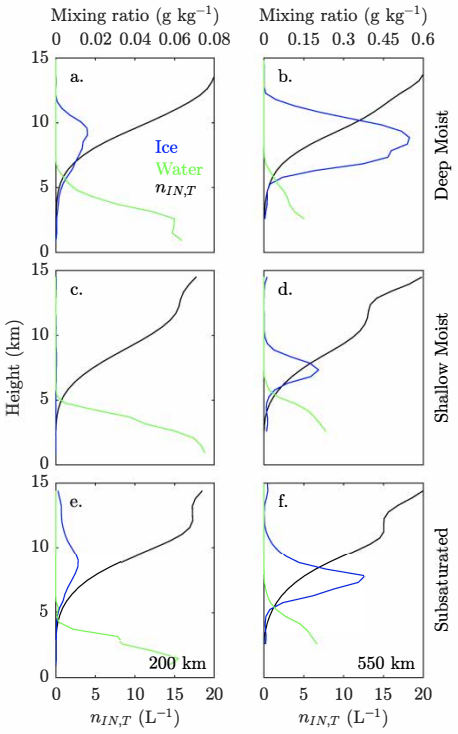

Figure 11. Vertical distribution of cloud ice (blue) and cloud droplets (green) in the (a)(b) deep moist, (c)(d) shallow moist, and (e)(f) subsaturated clusters at 200km (left) and 550km (right). Cloud ice has been multiplied by 100 so that it can be plotted on the same scale as cloud droplets. The black line shows $n_{IN,T}$. All panels are for the low dust scenario (INP0.5)

compared with the subsaturated case (0.3 mm-0.5 mm; Figure 13gi). For INP10 through INP100, the absolute changes in graupel in the subsaturated cluster represent a much higher relative change ranging from 10% to 20% averaged over the upwind slope of the peak (with maximum values as high as 30%). In contrast the changes in the deep moist case represent 5% to 10% increases in graupel. The changes in graupel over the peak are significant at higher INP concentratips (INP10 and INP100) in the subsaturated cluster, and for all INP concentrations in the deep moist cluster (Figure 14ghi). It is noteworthy that in the shallow moist and deep moist clusters, the variance in snow and graupel generally increases as the INP concentration increases, indicating that some cases within these clusters are highly sensitive to INPs, while others change relatively little.

These changes in precipitation can be traced to changes in the liquid water path (LWP) and ice water path (IWP), shown in Figure 15. The largest and most significant changes in LWP and IWP occur in the shallow moist case. This is driven by the relatively large amount of supercooled water in the low dust case being converted to snow. The smallest changes occur in the deep moist simulations, likely due to the fact that the input profiles are already at or near saturation through the mid-troposphere, and the relative lack of supercooled water in the low dust case. These changes follow a power-law relationship as a function of dust concentration (Figure 16), due to the functional relationship between n_{dust} and $n_{IN,T}$ (Equation 2). Changes in LWP are nearly equal and opposite to changes in IWP, indicating that the growth of ice is coming primarily at the expense of liquid water, rather than water vapor. LWP and IWP are most sensitive to dust at lower concentrations.

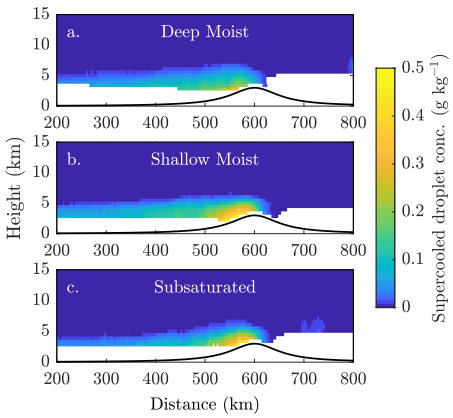

Figure 12. Vertical distribution of supercooled water droplets in the (a) deep moist, (b) shallow moist, and (c) subsaturated clusters for the low dust scenario (INP0.5)

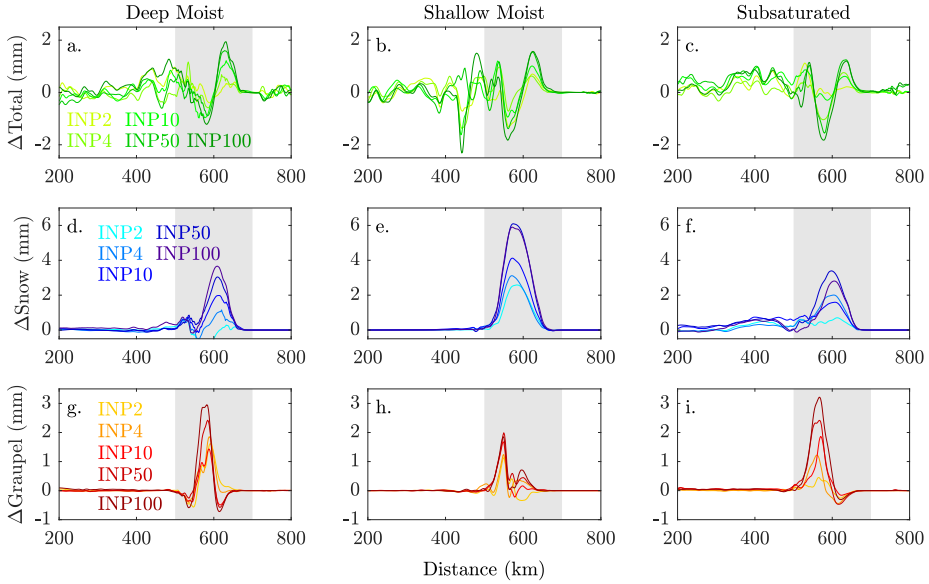

Figure 13. Changes in total precipitation ($\Delta Total$, top), snow ($\Delta Snow$, middle) and graupel ($\Delta Graupel$, bottom) for the (a)(d)(g) deep moist, (b)(e)(h) shallow moist, and (c)(f)(i) subsaturated clusters shown in Figure 3.

4 Model sensitivity

To assess the robustness of our results, we perform further analyses to examine the sensitivity to different modeling choices. In this section, we consider the effects of different ice nucleation parameterizations, model resolution, and the addition of a second mountain, analogous to the coastal range in California. Due to computational constraints, we perform these sensitivity tests on a subset of the 60 ensembles members used in the main body of the paper, selecting three radiosondes from each cluster.

The results presented above use the DeMott et al. (2010) ice nucleation parameterization (Equation 2), which was derived using measurements of ice nucleating particles from a series of observations mostly made over the Western US. Here we present a

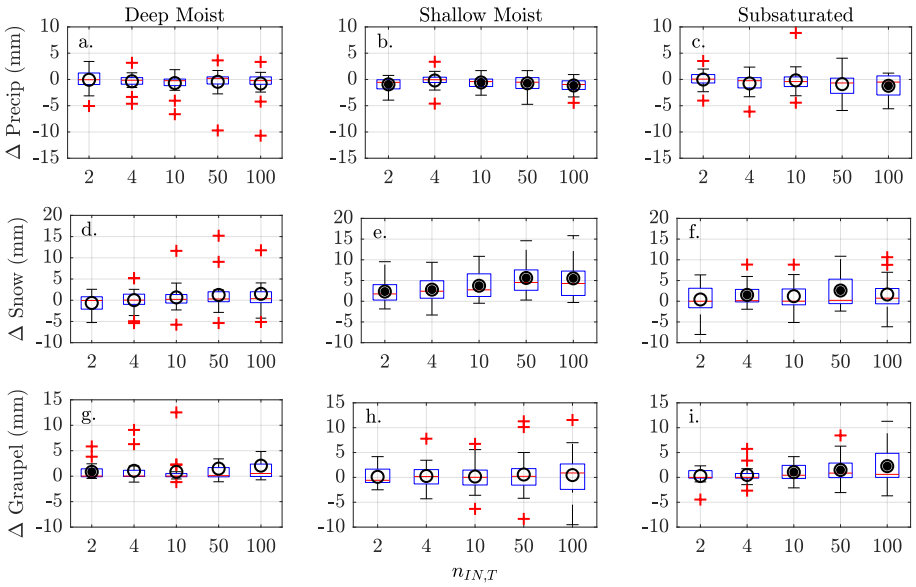

Figure 14. Boxplots show the ensemble spread of the change in precipitation, snow and graupel averaged over the peak (550km-650km) for the deep moist (adg), shallow moist (beh), and subsaturated clusters (cfi). Circles depict the ensemble means. Filled circles indicated that the mean is significantly different from 0 at the 95% confidence level using a student-T test.

comparison with the DeMott et al. (2015) ice nucleation parameterization:

$$n_{IN,T} = (cf)(n_{INP})^{(a(273.16-T)+b)} e^{(c(273.16-T)+d)} \tag{3}$$

where $n_{IN,T}$ is the number concentration of activated INP at temperature T, T is the environmental temperature (K), n_{INP} is the number concentration of INPs, and a, b, c, and d are empirically determined constants, and cf is a calibration factor. Here, $a = 0$, $b = 1.25$, $c = 0.46$, and $d = -11.6$. This parameterization was derived from laboratory based studies and is designed to provide a global approximation of dust effects on ice nucleation. We use a calibration factor of 3, as derived in DeMott et al. (2015) for atmospheric data. In a case study, this was also shown to provide good agreement with the Niemand et al. (2012) parameterization in a Saharan dust layer, although more work would be required to determine the relationship between these two parameterizations in a broader context (DeMott et al., 2015). At low dust concentrations Equation 2 and Equation 3 produce similar results, but $n_{IN,T}$ in Equation 3 is much more sensitive to higher values of n_{INP}, representing the higher ice nucleation activity of dust relative to other INPs. In the control case (INP0.5), the parameterization had very little effect on precipitation in the cases tested (Figure 17ab) as expected. At higher dust concentrations, the DeMott et al. (2015) parameterization lead to more ice being formed relative to DeMott et al. (2010). Comparing Figures 18 and Figure 19, we see larger increases in snow and graupel using the DeMott et al. (2015) parameterization and a more prominent spillover effect. Averaged on the upwind slope of the peak (550 km - 600 km), total precipitation decreases by -1.33 mm (INP2) to -2.65 mm (INP100) using the DeMott et al. (2010) parameterization, snow increases by 2.36 mm (INP2) to 8.37 mm (INP100), and graupel increases by 0.39 mm (INP2) to 3.36 mm (INP100). In contrast, using the DeMott et al. (2015) parameterization, precipitation decreases by -1.39 mm (INP2) to -4.37 mm (INP100), snow increases by 4.42 mm (INP2) to 17.75 mm (INP100), and graupel increases by 0.91 mm (INP2) to 4.44 mm (INP100). The differences between param-

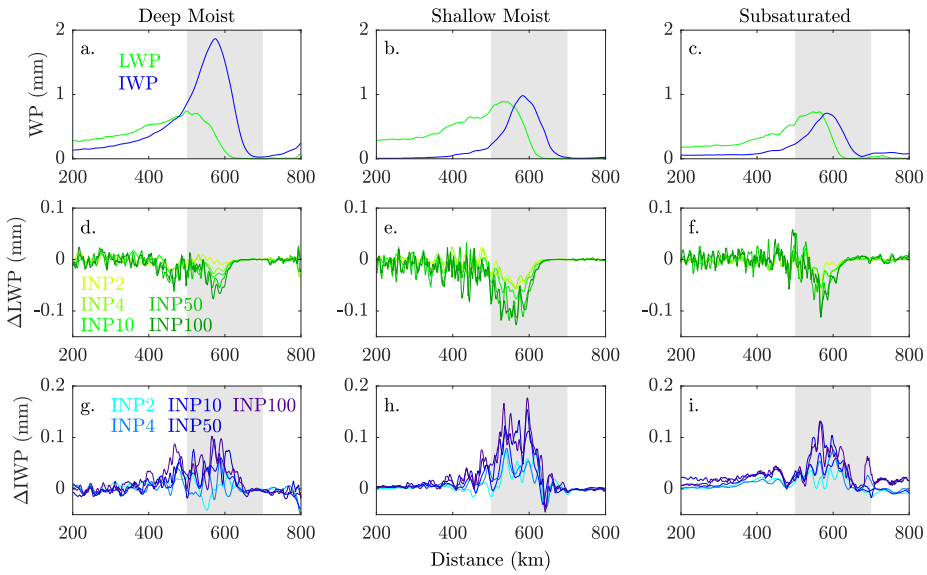

Figure 15. As in Figure 8, but with the ensemble members split into the (a)(d)(g) deep moist, (b)(e)(h) shallow moist, and (c)(f)(i) subsaturated clusters

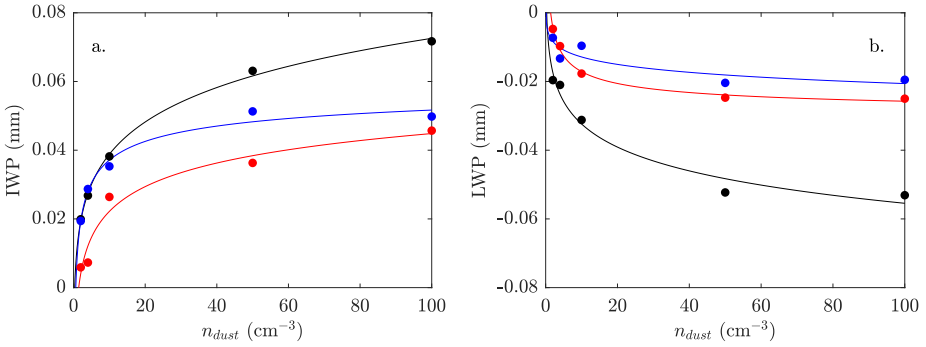

Figure 16. Changes (INPx-INP0.5) in IWP (a) and LWP (b) averaged over the peak (550km to 650km) as a function of dust concentration for the deep moist cluster (red), shallow moist cluster (black), and subsaturated cluster (blue).

eterizations are most prominent at high dust concentrations, but even at INP2, the changes in frozen precipitation (snow and graupel) are approximately doubled. The changes in precipitation agree qualitatively between the two parameterizations, but this suggests that the results presented in Section 3 may represent a lower bound on dust impacts on orographic precipitation.

Similarly, we tested the effects of model resolution by re-running the nine simulations described above, but with the horizontal resolution doubled to 1 km. The change in resolution had minimal effects on the control simulations (Figure 17c). Averaged over the upwind slope of the mountain (550 km - 600 km), total precipitation decreased by -0.86 mm (INP2) to -3.66 mm (INP100). Snow increased by 3.19 mm (INP2) to 14.92 mm (INP100), and graupel increased by 1.14 mm (INP2) to 4.66 mm (INP100). Compared with the low resolution simulation (Figure 19), these simulations have smaller changes in precipitation and snow, while graupel is slightly more sensitive to dust.

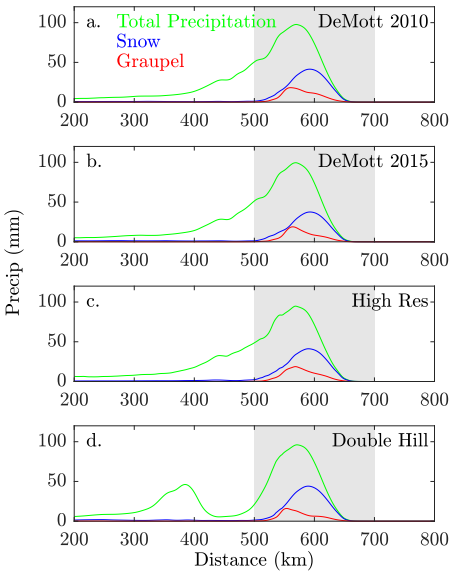

Figure 17. Ensemble mean (9 members) daily average total precipitation, snow, and graupel in the control scenario (INP0.5) using the (a) DeMott et al. (2010) ice nucleation parameterization (b) (DeMott et al., 2015) ice nucleation parameterization, (c) increased horizontal resolution (1km), and (d) a second small hill (500m) analogous to the California coastal range.

Finally, while our goal in this paper has been to present results that are generalizable beyond the US West Coast, the West Coast does have important terrain features that may have an effect on our results. To test the robustness of our results, we performed an experiment where we added a coastal mountain range, with a height of 500 m, centered at 400 km from the western boundary. The addition of the small hill produced a secondary peak in total precipitation centered over the hill that is composed entirely of rain (as opposed to snow or graupel; Figure 17a,d). This had a relatively small impact, except at high dust concentrations (INP50-100, compare Figure 19 and Figure 21). Total precipitation over the upwind slope of the 3000 m peak decreases by -1.15 mm (INP2) to -3.21 mm (INP100) and snow increases by 2.14 mm (INP2) to 11.03 mm (INP100). Compared with the changes in the single hill simulations, this represents a slight decrease in the dust sensitivity of snow and total precipitation. The increase in graupel falling on the upwind slope of the 3000 m peak was similar to the single hill simulations in the low dust simulations (0.83 mm for INP2), but at high dust concentrations, graupel was more sensitive to dust under the two hill scenario (6.32 mm at INP100).

5 Discussion

Overall, the effects of dust on total precipitation were relatively small (generally $\leq 1.5\%$ upwind of the peak, Figure 7b), but we did find that dust had a large effect on precipitation type (Figure 7cd), leading to increases in both snow and graupel (as much as 10% upwind of the peak at the highest dust concentrations) in our idealized simulations. The ability to accurately forecast the snow/rain ratio during landfalling atmospheric rivers has important implications for water resource management (Dettinger et al., 2011; Ralph et al., 2019). Additionally, the snow/rain ratio is important for understanding flood risks both during and after events. When more of the precipitation falls as rain, it will increase the risk of flooding during the AR (Lundquist et al., 2008), although at the same time, a higher ratio falling as snow could create antecedent conditions that would lead

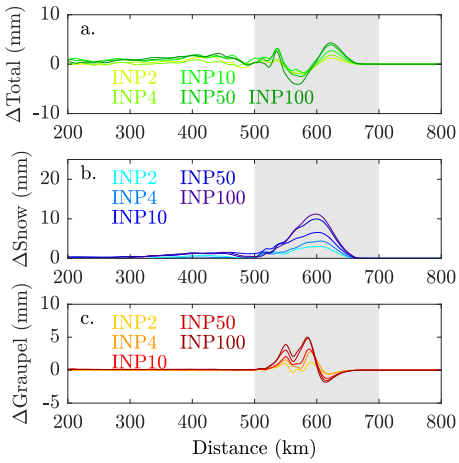

Figure 18. Ensemble mean (9 members) change in (a) total precipitation, (b) snow, and (c) graupel (INPx-INP0.5) using the (DeMott et al., 2010) ice nucleation parameterization.

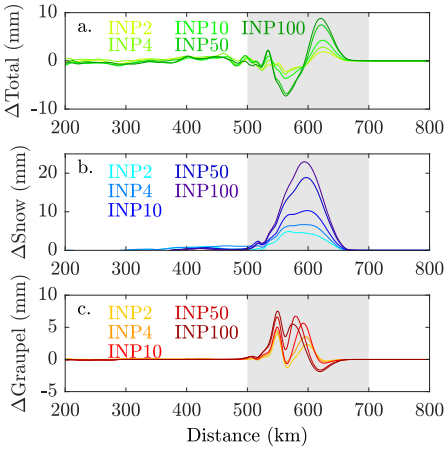

Figure 19. Ensemble mean (9 members) change in (a) total precipitation, (b) snow, and (c) graupel (INPx-INP0.5) using the (DeMott et al., 2015) ice nucleation parameterization.

to greater flood risks during subsequent events (Kattelmann, 1997). The increases in precipitation on the lee side of the peak, sometimes referred to as a "spillover" effect also provide an important source of water for areas to the east of the mountain.

In general, the relationship between dust concentration and LWP and IWP follows a power law relationship, and is most sensitive at lower concentration levels (INP <10, Figure 16), resulting in a non-linear precipitation response (Figure 7bcd). This suggests that at higher dust concentrations, moisture availability becomes the determining factor for ice formation, rather than temperature. We found that the sondes that we classified as "shallow moist" were most sensitive to changes in dust concentrations (Figure 13, Figure 16). In these cases, the environment was on average colder than other sondes, with a moist layer near the surface that is capped in the lower troposphere. Unlike the deep moist sondes, which tended to be saturated throughout the mid-troposphere, or the subsaturated sondes which are below saturation throughout most of the tropo-

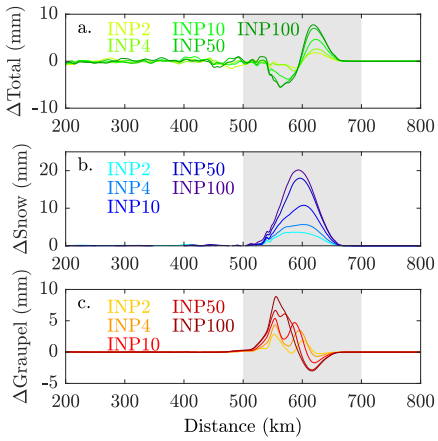

Figure 20. Ensemble mean (9 members) change in (a) total precipitation, (b) snow, and (c) graupel (INPx-INP0.5) using the (DeMott et al., 2015) ice nucleation parameterization, and with the horizontal resolution increased to 1km.

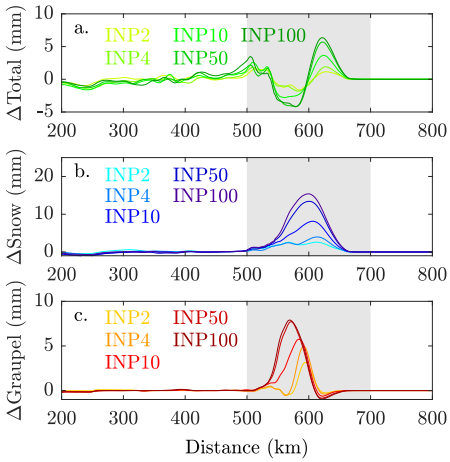

Figure 21. Ensemble mean (9 members) change in (a) total precipitation, (b) snow, and (c) graupel (INPx-INP0.5) using the (DeMott et al., 2015) ice nucleation parameterization, with a second hill (500 m) added centered 400 km from the western boundary.

sphere, these sondes only become subsaturated near the freezing level. As such, adding dust (which effectively increases the temperatures at which ice can form in the model), will have a large impact on the amount of moisture that is available for ice nucleation. The shallow moist sondes represent conditions on the periphery of atmospheric rivers. Eleven of the 20 sondes that were included in the shallow moist cluster occurred on or after the passage of the cold front at Bodega Bay (not shown), indicating that precipitation occurring along with the cold front may be especially responsive to dust. In addition, previous research has indicated that the cold sector of a storm is the region where dust is most likely to be present (Creamean et al., 2013). While the bulk of precipitation during an AR typically falls prior to the passage of the cold front, narrow cold frontal rainbands produce short duration intense precipitation that has been associated with hazardous debris flow (Oakley et al., 2017). The potential role of atmospheric dust in con-

tributing to these brief intense precipitation events should be evaluated in future studies.

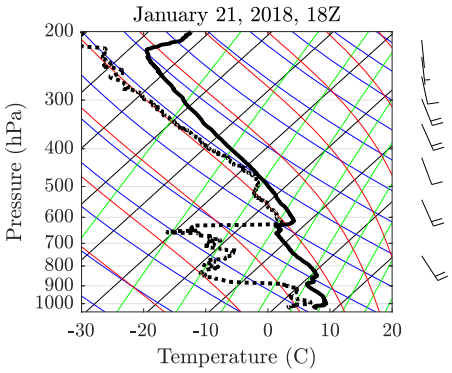

Figure 22. Skew-T for the radiosonde launched from Bodega Bay on January 21, 2018 at 18Z.

Previous modeling and observational studies have found that in some cases increased dust concentrations can lead to increases in total precipitation (rain and snow) via the seeder-feeder mechanism (Ault et al., 2011; Creamean et al., 2013; Fan et al., 2014, 2017). Our model is unable to reproduce this result in the ensemble mean. Although increasing dust leads to increasing snowfall over the mountain (Figure 7c), total precipitation decreases upwind of the peak (Figure 7b). The only increases in total precipitation occurred on the downwind slope of the peak, where most of the precipitation fell as snow in the control simulation (Figure 7b). However, a few individual ensemble members did produce increases in total precipitation. Figure 22 was the first radiosonde collected during a January 21-22, 2018 AR event, and was classified as subsaturated in our clustering. This sonde was relatively cold in the lower atmosphere and has a pronounced dry layer from 900-750 hPa. Notably, this radiosonde has the most pronounced dry layer of all the radiosondes collected during the 2017-2018 FIRO campaign. This dry layer is an important element of a typical seeder-feeder environment because it indicates that the high cloud is decoupled from the low cloud (Schneider & Moneypenny, 2002; Thompson et al., 2004). In this case, the initial conditions were cold enough that the model produced snow upwind of the mountain in the control simulation (Figure 23a). Figure 24ab shows the vertical distribution of cloud ice, cloud water, snow and graupel in the low dust simulation at 200 km. Ice is concentrated in the layer between 5-10 km. Below 5 km, ice develops into snow and graupel and begins to precipitate out. As shown in Figure 23bc, when dust is added to the simulation, it increases snow on the upwind slope of the mountain (400 km-600 km) by 4.37 mm - 6.10 mm (INP2.0 - INP100) and total precipitation by 4.40 mm - 6.57 mm (INP2.0 - INP100). Graupel goes from nearly non-existent in the low dust concentrations (control, INP2, INP4) to 1 mm - 2 mm in the higher dust concentrations (INP10 - INP100, Figure 23d). Focusing on INP10, there is a large increase in cloud ice in the mid troposphere, and a corresponding increase in snow and graupel (Figure 24cd). However, in this case, there is also an increase in cloud water near the surface. This suggests that some of the frozen precipitation (snow and graupel) melted in this layer. This process resembles the seeder-feeder mechanism, wherein precipitation in the low cloud is fed by snow and ice falling from a higher cloud (Creamean et al., 2013). This supports the interpretation that the seeder feeder mechanism is most important during the beginning and end of the event, which is not necessarily well represented by the FIRO radiosondes as the project focused on peak AR intensity.

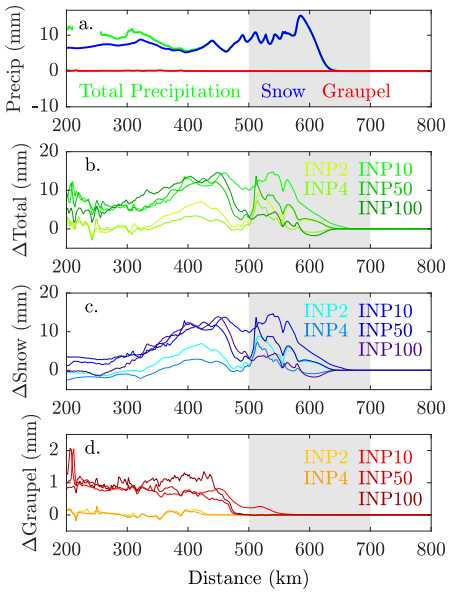

Figure 23. (a) Daily average precipitation, snow and graupel in the control scenario forced by the sonde in Figure 22. Changes in daily average (b) precipitation, (c) snow, and (d) graupel (as in Figure 7b) for the single ensemble member.

6 Conclusions

Atmospheric Rivers can provide as much as 50% of the annual precipitation to the U.S. West Coast, and depending on their intensity can range from being mostly beneficial to extremely hazardous (Ralph et al., 2019). As such, accurately forecasting AR precipitation is extremely important for California's water management. Dust and other INPs affect precipitation during AR events by acting as ice nuclei. This directly affects the formation of snow, and so can alter the rain/snow ratio which has significance for both water management and assessing flood risk. Further, Creamean et al. (2013) showed observational evidence that dust can produce more intense precipitation through the "seeder-feeder" mechanism, in which snow and ice form in a upper-level "seeder" cloud and then fall through a low-level "feeder" cloud, producing larger rain drops and graupel.

In this study, we use a theoretical modeling framework to test the sensitivity of orographic precipitation to heightened dust concentrations under a broad range of initial conditions. We found that increasing dust increased the percentage of total precipitation that was falling as frozen precipitation (snow and graupel). The slower fall speeds of snow relative to liquid rain produced a spillover effect, where total precipitation decreased upwind of the peak and increased in the lee of the peak. The modeled precipitation was most sensitive to dust when it was initiated with "shallow moist" conditions, which primarily occurred at the beginning and end of AR events. In general, the modeled sensitivity to dust followed a power law relationship, as predicted by Equation 2.

In order to test the robustness of our results, we ran a smaller ensemble and tested the effects of using a different ice nucleation parameterization, increasing the model resolution, and adding a second, smaller hill similar to the California coastal range. We found that using the DeMott et al. (2015) ice nucleation parameterization lead to the model being far more sensitive to changes in dust. In particular, the increases in snow caused by dust approximately doubled compared with the DeMott et al. (2010) parameteriza-

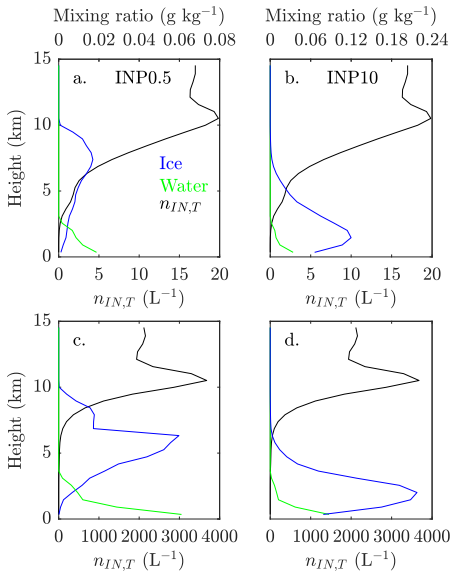

Figure 24. (a)(c)Vertical distribution of cloud ice (blue) and cloud droplets (green) at 200km for the radiosonde launched from Bodega Bay on January 21, 2018 at 18Z. Cloud ice is multiplied by 100 so that it can be plotted on the same scale as cloud droplets. (b)(d) Vertical distribution of total frozen precipitation (snow, graupel, and ice; blue) and total cloud water (rain and cloud drops; green). Frozen (liquid) precipitation is predominantly snow (rain). The black line shows $n_{IN,T}$. The top plots (a)(b) show INP0.5. The bottom plots (c)(d) show INP10.

tion. Increasing the model resolution had a smaller impact, but did lead to a small increase (decrease) in the sensitivity of graupel (snow) at high dust concentrations. Similarly, adding a second 500 m hill to the model also lead to an increase (decrease) in the sensitivity of graupel (snow) at high dust concentrations.

As we have shown here, dust is important for determining the snow/rain ratio during atmospheric rivers, particularly at the early and late stages of the event, and in individual cases may have a large impact on overall precipitation. However, further research is needed to fully understand the effects of dust on orographic precipitation during landfalling atmospheric rivers. This study neglects the role of large scale dynamics, in particular the Sierra barrier jet, which is expected to contribute to the seeder-feeder mechanism by dissociating the upper level seeder cloud and the lower level feeder cloud. In this work, we assumed a constant vertical profile of dust. In the real atmosphere dust is transported across the Pacific in discrete layers, and we expect the altitude of the dust layer to affect the precipitation response (Ault et al., 2011; Creamean et al., 2013). In addition, further studies will be needed to test the robustness of these results to different model configurations, such as using a more computational expensive spectral bin microphysics scheme, rather than the Thompson Aerosol Aware microphysics. Finally, in order to better validate the results of this work we will need to obtain collocated observations of vertical profiles of dust (and other ice nucleating particles), temperature, humidity, and hydrometeors during landfalling atmospheric rivers.

Acknowledgments

The authors would like to thank Kara Voss and Andrew Martin for their contributions to this project. All FIRO radiosondes can be found at `ftp://sioftp.ucsd.edu/CW3E_DataShare/CW3E_Radiosondes`. This work was funded by the California Department

of Water Resources contract 4600010378, Task Order OSCOP215 and the Army Corps of Engineers USACE (CESU) W912HZ-15-0019.

References

Atkinson, J. D., Murray, B. J., Woodhouse, M. T., Whale, T. F., Baustian, K. J., Carslaw, K. S., ... Malkin, T. L. (2013). The importance of feldspar for ice nucleation by mineral dust and mixed-phase clouds. *Nature*, *498*, 355-358.

Ault, A. P., Williams, C. R., White, A. B., Neiman, P. J., Creamean, J. M., Gaston, C. J., ... Prather, K. A. (2011). Detection of Asian dust in California orographic precipitation. *Journal of Geophysical Research*, *116*, D16205.

Bigg, E. K. (1953). The formation of atmospheric ice crystals by the freezing of droplets. *Quarterly Journal of the Royal Meteorological Society*, *79*(342), 510-519.

Colle, B. (2004). Sensitivity of orographic precipitation to changing ambient conditions and terrain geometries: An idealized modeling perspective. *Journal of Atmospheric Science*, *61*, 588-606.

Colle, B., & Mass, C. F. (2000). The 5–9 february 1996 flooding event over the pacific northwest: Sensitivity studies and evaluation of the mm5 precipitation forecasts. *Monthly Weather Review*, *128*(3), 593-617.

Colle, B. A., Garvert, M. F., Wolfe, J. B., Mass, C. F., & Woods, C. P. (2005). The 13–14 december 2001 improve-2 event. part iii: Simulated microphysical budgets and sensitivity studies. *Journal of Atmospheric Science*, *62*(10), 3535–3558.

Colle, B. A., & Zeng, Y. (2004). Bulk microphysical sensitivities within the mm5 for orographic precipitation. part ii: Impact of barrier width and freezing level. *Monthly Weather Review*, *132*(12), 2802-2815.

Copernicus Climate Change Service (C3S). (2017). *ERA5: Fifth generation of ECMWF atmospheric reanalyses of the global climate.* Retrieved February 9, 2019, from `https://cds.climate.copernicus.eu/cdsapp#!/home`

Cordeira, J. M., Ralph, F. M., Martin, A., Gaggini, N., Spackman, J. R., Neiman, P. J., ... Pierce, R. (2017). Forecasting atmospheric rivers during calwater 2015. *Bulletin of the American Meteorological Society*, *98*(3), 449-459.

Cornwell, G. C., McCluskey, C. S., Levin, E. J. T., Suski, K. J., DeMott, P. J., Kreidenweis, S. M., & Prather, K. A. (2019). Direct online mass spectrometry measurements of ice nucleating particles at a california coastal site. *Journal of Geophysical Research Atmospheres*, *124*, 12157-12172.

Creamean, J. M., Ault, A. P., White, A. B., Neiman, P. J., Ralph, F. M., Minnis, P., & Prather, K. A. (2015). Impact of interannual variations in sources of insoluble aerosol species on orographic precipitation over california's central sierra nevada. *Atmospheric Chemistry and Physics*, *15*, 6535-6548.

Creamean, J. M., Spackman, J. R., Davis, S. M., & White, A. B. (2014). Climatology of long-range transported asian dust along the west coast of the united states. *Journal of Geophysical Research Atmospheres*, *119*, 12171-12185.

Creamean, J. M., Suski, K. J., Rosenfeld, D., Cazorla, A., DeMott, P. J., Sullivan, R. C., ... Prather, K. A. (2013). Dust and biological aerosols from the Sahara and Asia influence precipitation in the Western U.S. *Science*, *339*, 1572-1578.

Creamean, J. M., White, A. B., Minnis, P., Palikonda, R., Spangenberg, D. A., & Prather, K. A. (2016). The relationships between insoluble precipitation residues, clouds, and precipitation over california's southern sierra nevada during winter storms. *Atmospheric Environment*, *140*, 298-310.

DeMott, P. J., Prenni, A. J., Liu, X., Kreidenweis, S. M., Petters, M. D., Twohy, C. H., ... Rogers, D. C. (2010). Predicting global atmospheric ice nuclei distributions and their impacts on climate. *Proceedings of the National Academy of Sciences*, *107*(25), 11217-11222.

DeMott, P. J., Prenni, A. J., McMeeking, G. R., Sullivan, R. C., Petters, M. D., Tobo, Y., ... Kreidenweis, S. M. (2015). Integrating laboratory and field data to quantify the immersion freezing ice nucleation activity of mineral dust particles. *Atmospheric Chemistry and Physics*, *15*, 393-409.

DeMott, P. J., Sassen, K., Poellot, M. R., Baumgardner, D., Rogers, D. C., Brooks, S. D., ... Kreidenweis, S. M. (2003). African dust aerosols as atmospheric ice nuclei. *Geophysical Research Letters*, *30*, 1732.

Dettinger, M. D., Ralph, F. M., Das, T., & Neiman, P. J. (2011). Atmospheric rivers, floods and the water resources of California. *Water*, *3*(2), 445-478.

Fan, J., Leung, L. R., DeMott, P. J., Comstock, J. M., Singh, B., Rosenfeld, D., ... Min, Q. (2014). Aerosol impacts on California winter clouds and preicpitation during CalWater 2011: local pollution versus long-range transported dust. *Atmospheric Chemistry and Physics*, *14*, 81-101.

Fan, J., Leung, L. R., Rosenfeld, D., & DeMott, P. J. (2017). Effects of cloud condensation nuclei and ice nucleating particles on precipitation processes and supercooled liquid in mixed-phase orographic clouds. *Atmospheric Chemistry and Physics*, *17*, 1017-1035.

Hallett, J., & Mossop, S. C. (1974). Production of secondary ice particles during the riming process. *Nature*, *249*, 26-28.

Hande, L. B., Engler, C., Hoose, C., & Tegen, I. (2015). Seasonal variability of saharan desert dust and ice nucleating particles over europe. *Atmospheric Chemistry and Physics*, *15*, 4389-4397.

Heintzenberg, J., Okada, K., & Strom, J. (1996). On the composition of non-volatile material in upper tropospheric aerosols and cirrus crystals. *Atmospheric Research*, *41*, 81-88.

Jasperse, J., Ralph, F. M., Anderson, M., Brekke, L. D., Dillabough, M., Dettinger, M. D., ... Webb, R. H. (2017). *Preliminary viability assessment of lake mendocino forecast informed reservoir operations* (Tech. Rep.). Center for Western Weather and Water Extremes.

Kattelmann, R. (1997). Flooding from rain-on-snow events in the sierra nevada. In G. H. Leavesley (Ed.), *Destructive water: Water-caused natural disasters, their abatement and control* (Vol. 239, p. 59-65). IAHS.

Koop, T., Luo, B. P., Tsias, A., & Peter, T. (2000). Water activity as the determinant for homogeneous ice nucleation in aqueous solutions. *Nature*, *406*, 611-614.

Levin, E. J. T., DeMott, P. J., Suski, K. J., Boose, Y., Hill, T. C. J., McCluskey, C. S., ... Kreidenweis, S. M. (2019). Characteristics of ice nucleating particles in and around california winter storms. *Journal of Geophysical Research Atmospheres*, *124*, 11530-11551.

Lundquist, J. D., Neiman, P. J., Martner, B., White, A. B., Gottas, D. J., & Ralph, F. M. (2008). Rain versus snow in the Sierra Nevada, California: Comparing doppler profiling radar and surface observations of melting level. *Journal of Hydrometeorology*, *9*, 194-211.

Martin, A., Cornwell, G., Beall, C. M., Cannon, F., Reilly, S., Schaap, B., ... Prather, K. A. (2019). Contrasting local and long-range-transported warm ice-nucleating particles during an atmospheric river in coastal california, usa. *Atmospheric Chemistry and Physics*, *19*, 4193-4210.

Morales, A., Morrison, H., & Posselt, D. J. (2018). Orographic precipitation response to microphysical parameter perturbations for idealized moist nearly neutral flow. *Journal of Atmospheric Science*, *75*(6), 1933-1955.

Niemand, M., Moehler, O., Vogel, B., Vogel, H., Hoose, C., Connolly, P., ... Leisner, T. (2012). Parameterization of immersion freezing on mineral dust particles: An application in a regional scale model. *Journal of Atmospheric Science*, *69*(3077-3092).

Oakley, N. S., Lancaster, J. T., Kaplan, M. L., & Ralph, F. M. (2017). Synoptic

conditions associated with cool season post-fire debris flows in the Transverse Ranges of southern California. *Natural Hazards*, *88*, 327-354.

Ralph, F. M., Coleman, T., Neiman, P. J., Zamora, R. J., & Dettinger, M. D. (2013). Observed impacts of duration and seasonality of atmospheric-river landfalls on soil moisture and runoff in coastal Northern California. *Journal of Hydrometeorology*, *14*, 443-459.

Ralph, F. M., Neiman, P. J., & Wick, G. A. (2004). Satellite and caljet aircraft observations of atmospheric rivers over the eastern north pacific ocean during the winter of 1997/1998. *Monthly Weather Review*, *132*, 1721-1745.

Ralph, F. M., Neiman, P. J., Wick, G. A., Gutman, S. I., Dettinger, M. D., Cayan, D. R., & White, A. B. (2006). Flooding on California's Russian River: Role of atmospheric rivers. *Geophysical Research Letters*, *33*, L13801.

Ralph, F. M., Prather, K. A., Cayan, D., Spackman, J. R., DeMott, P., Dettinger, M., ... Intrieri, J. (2016). Calwater field studies designed to quantify the roles of atmospheric rivers and aerosols in modulating u.s. west coast precipitation in a changing climate. *Bulletin of the American Meteorological Society*, *97*(7), 1209-1228. Retrieved from `https://doi.org/10.1175/BAMS-D-14-00043.1` doi: 10.1175/BAMS-D-14-00043.1

Ralph, F. M., Rutz, J. J., Cordeira, J. M., Dettinger, M. D., Anderson, M., Reynolds, D., ... Smallcomb, C. (2019). A scale to characterize the strength and impacts of atmospheric rivers. *Bulletin of the American Meteorological Society*, *100*, 269-289.

Reisner, J., Rasmussen, R. M., & Bruintjes, R. T. (1998). Explicit forecasting of supercooled liquid water in winter storms using the mm5 mesoscale model. *Quarterly Journal of the Royal Meteorological Society*, *124*, 1071-1107.

Rutz, J. J., Steenburgh, W. J., & Ralph, F. M. (2014). Climatological characteristics of atmospheric rivers and their inland penetration over the Western United States. *Monthly Weather Review*, *142*, 905-921.

Schneider, D., & Moneypenny, M. (2002). The mesoscale seeder-feeder mechanism: Its forecast implications. *National Weather Digest*, *26*(12), 45-52.

Skamarock, W. C., Klemp, J. B., Dudhia, J., Gill, D. O., Barker, D. M., Duda, M. G., ... Powers, J. G. (2008). *A description of the Advanced Research WRF Version 3* (Tech. Rep. Nos. No. NCAR/TN-475+STR). Boulder, Colorado, USA: National Center of Atmospheric Research.

Thompson, G., & Eidhammer, T. (2014). A study of aerosol impacts on clouds and precipitation development in a large winter cyclone. *Journal of Atmospheric Science*, *71*, 3636-3658.

Thompson, G., Field, P. R., Rasmussen, R. M., & Hall, W. D. (2008). Explicit forecasts of winter precipitation using an improved bulk microphysics scheme. part ii: Implementation of a new snow parameterization. *Monthly Weather Review*, *136*, 5095-5115.

Thompson, G., Rasmussen, R. M., & Manning, K. (2004). Explicit forecasts of winter precipitation using an improved bulk microphysics scheme. part i: Description and sensitivity analysis. *Monthly Weather Review*, *132*, 519-542.

Vali, G., DeMott, P. J., Mohler, O., & Whale, T. F. (2015). Technical note: A proposal for ice nucleation terminology. *Atmospheric Chemistry and Physics*, *15*, 10263-10270.

Wallmann, J., & Milne, R. (2007). *Forecasting lee-side precipitation in the central and northern sierra nevada part i: Instability and wind* (Tech. Rep. No. 07-01). National Weather Service.

Weather Prediction Center. (2019, 11). *Wpc surface analysis archive.* Retrieved November 25, 2019, from `https://www.wpc.ncep.noaa.gov/archives/web_pages/sfc/sfc_archive.php`

Zhu, Y., & Newell, R. E. (1998). A proposed algorithm for moisture fluxes from atmospheric rivers. *Monthly Weather Review*, *126*, 725-735.

Figure 1.

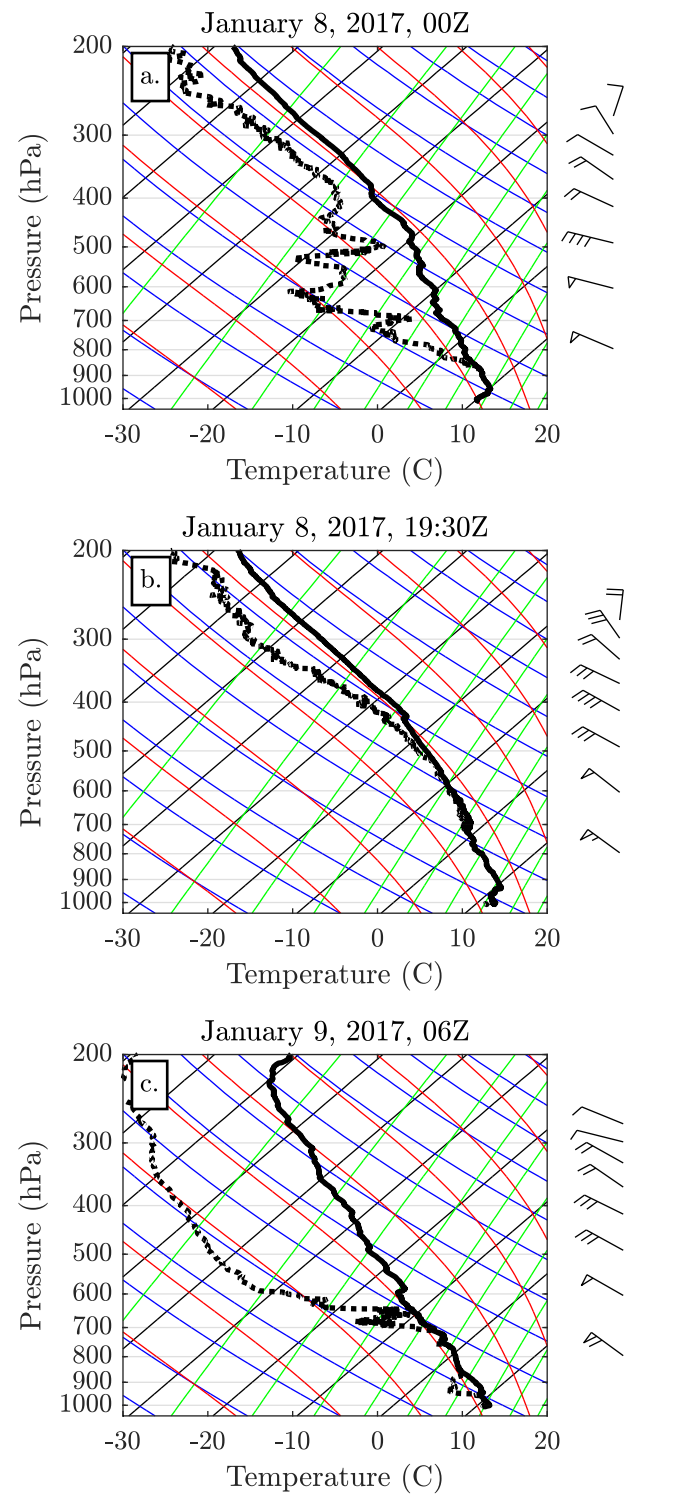
January 8, 2017, 00Z
a.
Pressure (hPa)
200
300
400
500
600
700
800
900
1000
-30
-20
-10
0
10
20
Temperature (C)
January 8, 2017, 19:30Z
b.
Pressure (hPa)
Temperature (C)
January 9, 2017, 06Z
c.
Pressure (hPa)
Temperature (C)

Figure 2.

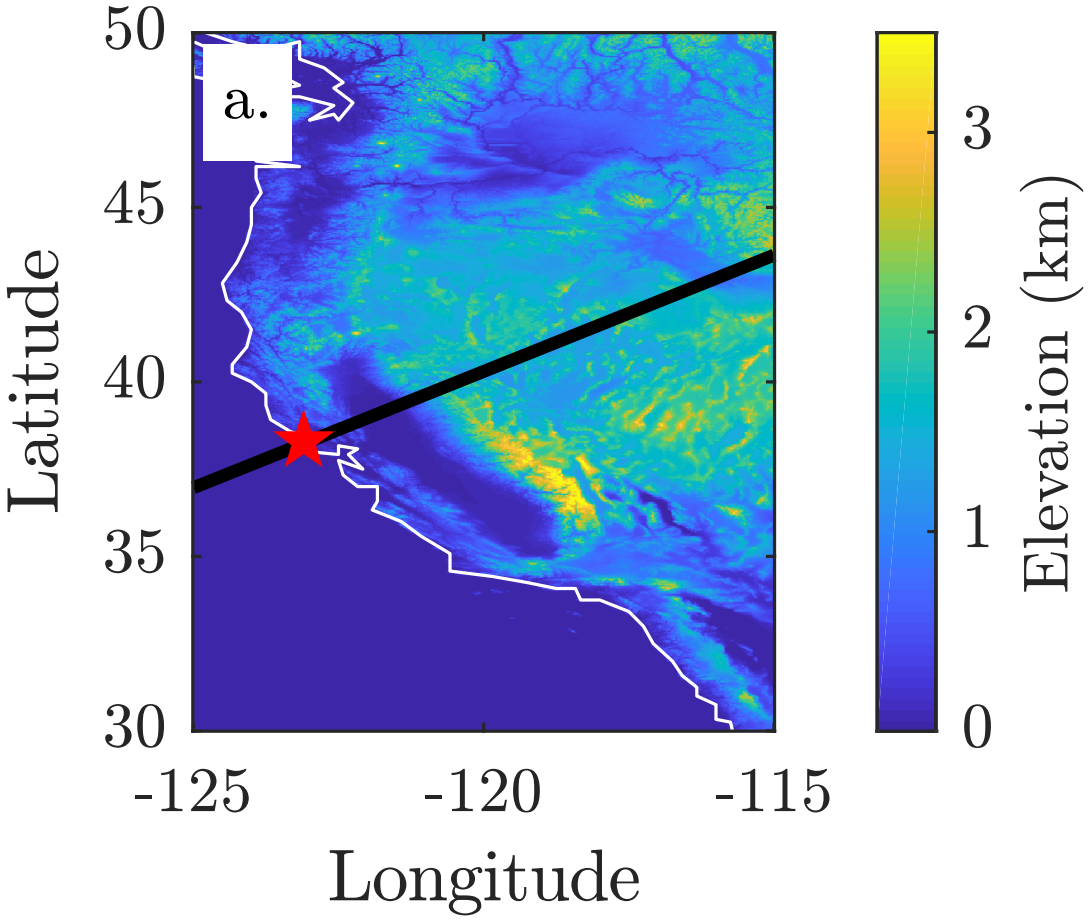
a.
50
45
40
35
30
Latitude
-125
-120
-115
Longitude
3
2
1
0
Elevation (km)

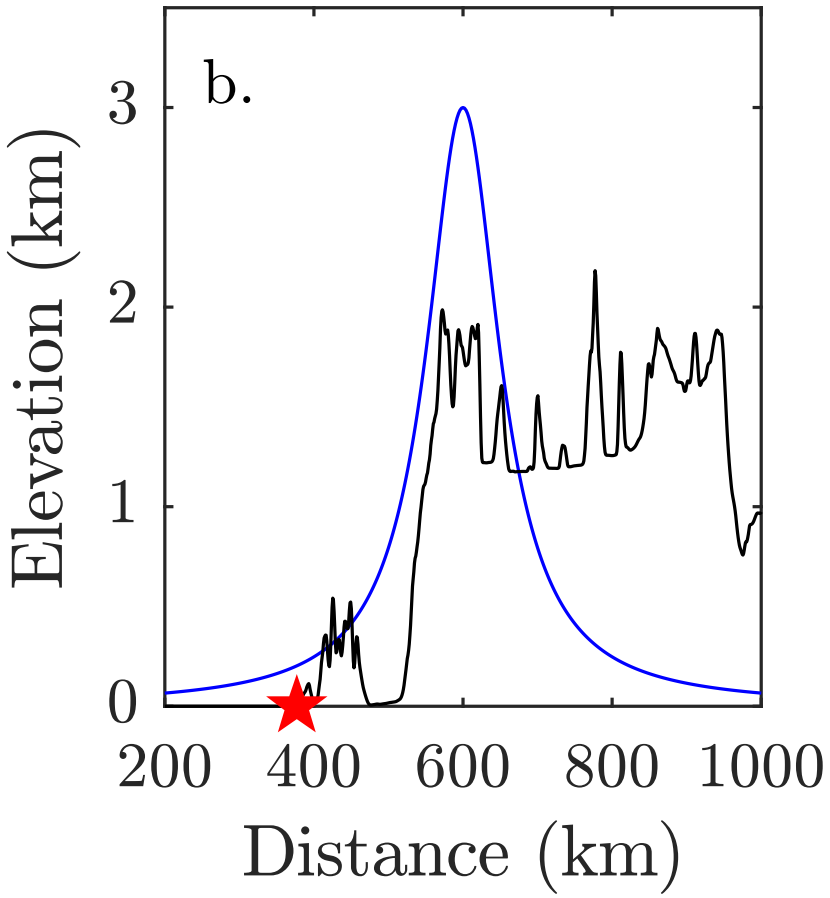
b.
3
2
1
0
Elevation (km)
200
400
600
800
1000
Distance (km)

Figure 3.

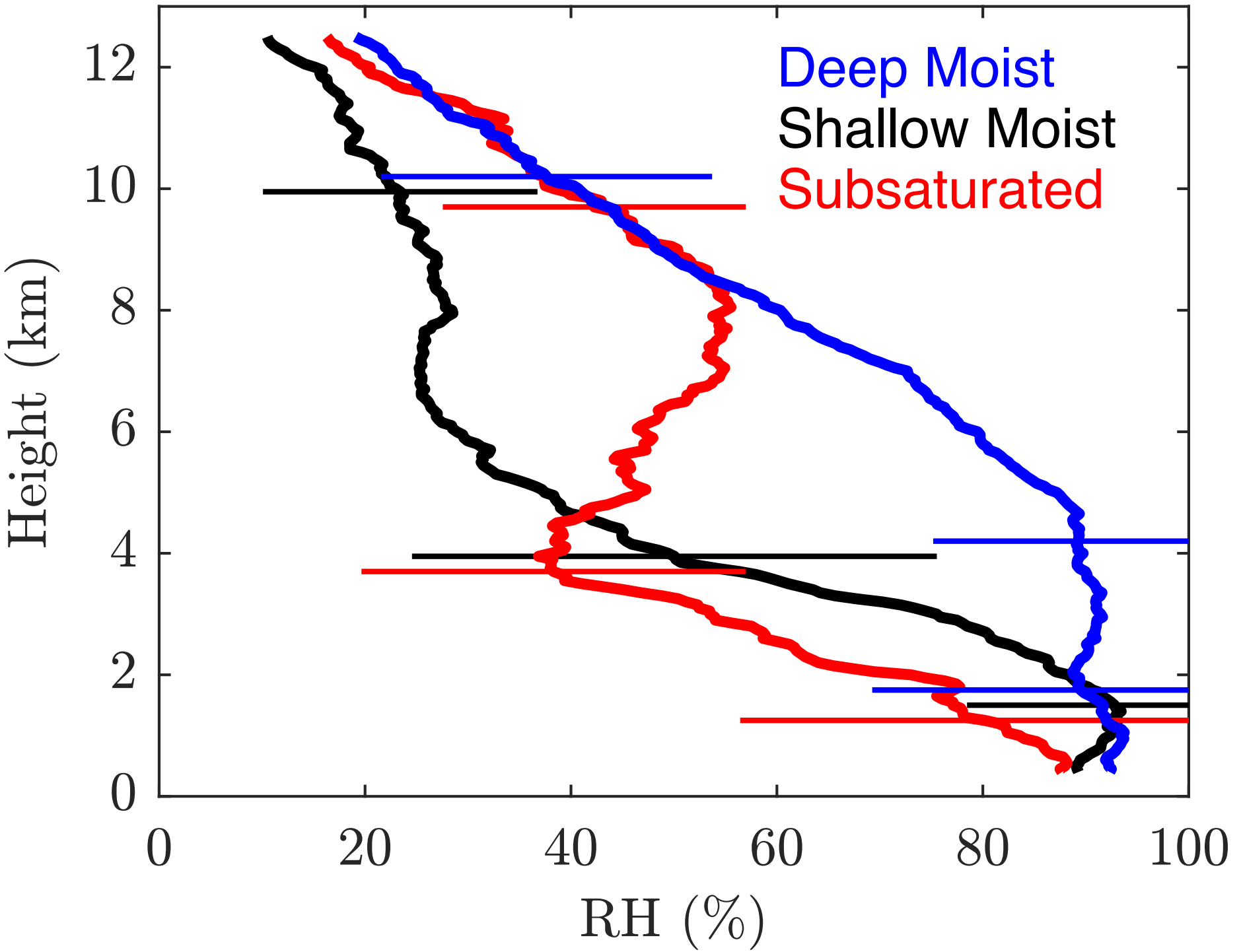
Deep Moist
Shallow Moist
Subsaturated
Height (km)
RH (%)
0
2
4
6
8
10
12
0
20
40
60
80
100

Figure 4.

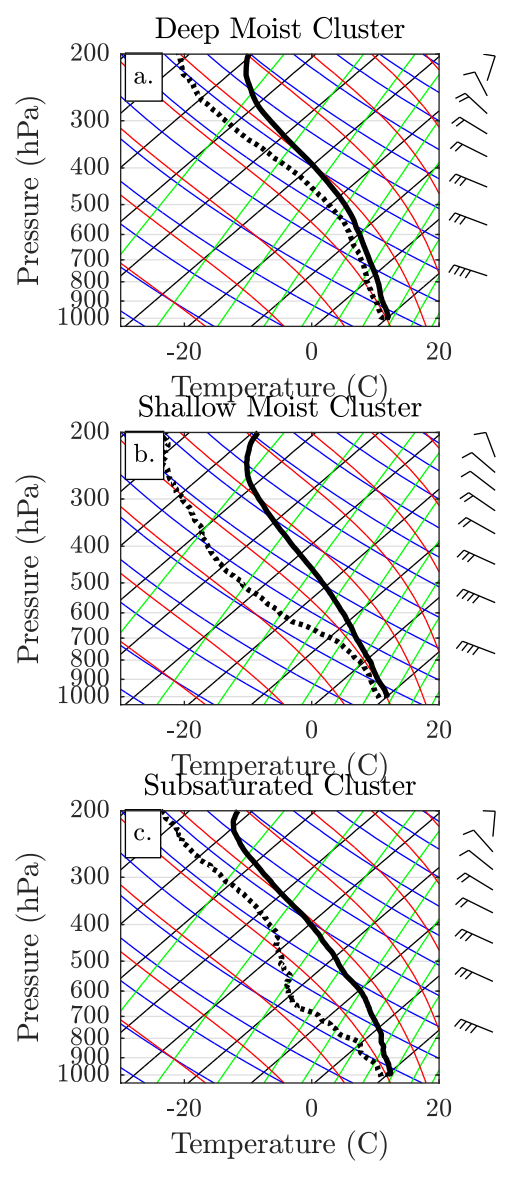
Deep Moist Cluster
a.
Shallow Moist Cluster
b.
Subsaturated Cluster
c.
Pressure (hPa)
200
300
400
500
600
700
800
900
1000
-20
0
20
Temperature (C)

Figure 5.

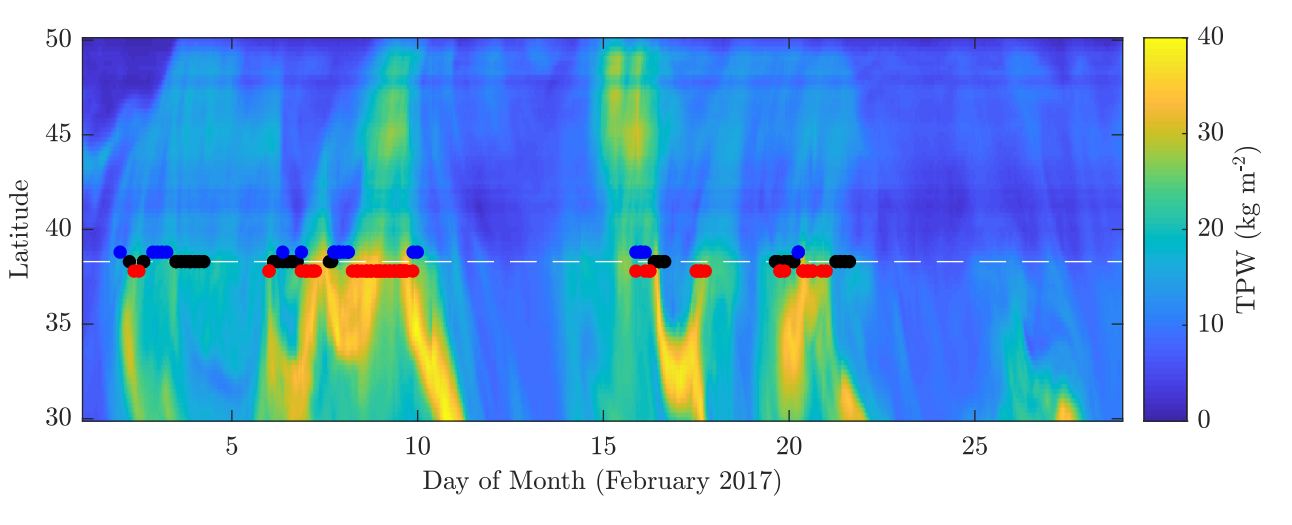
Latitude
50
45
40
35
30
5
10
15
20
25
Day of Month (February 2017)
40
30
20
10
0
TPW (kg m-2)

Figure 6.

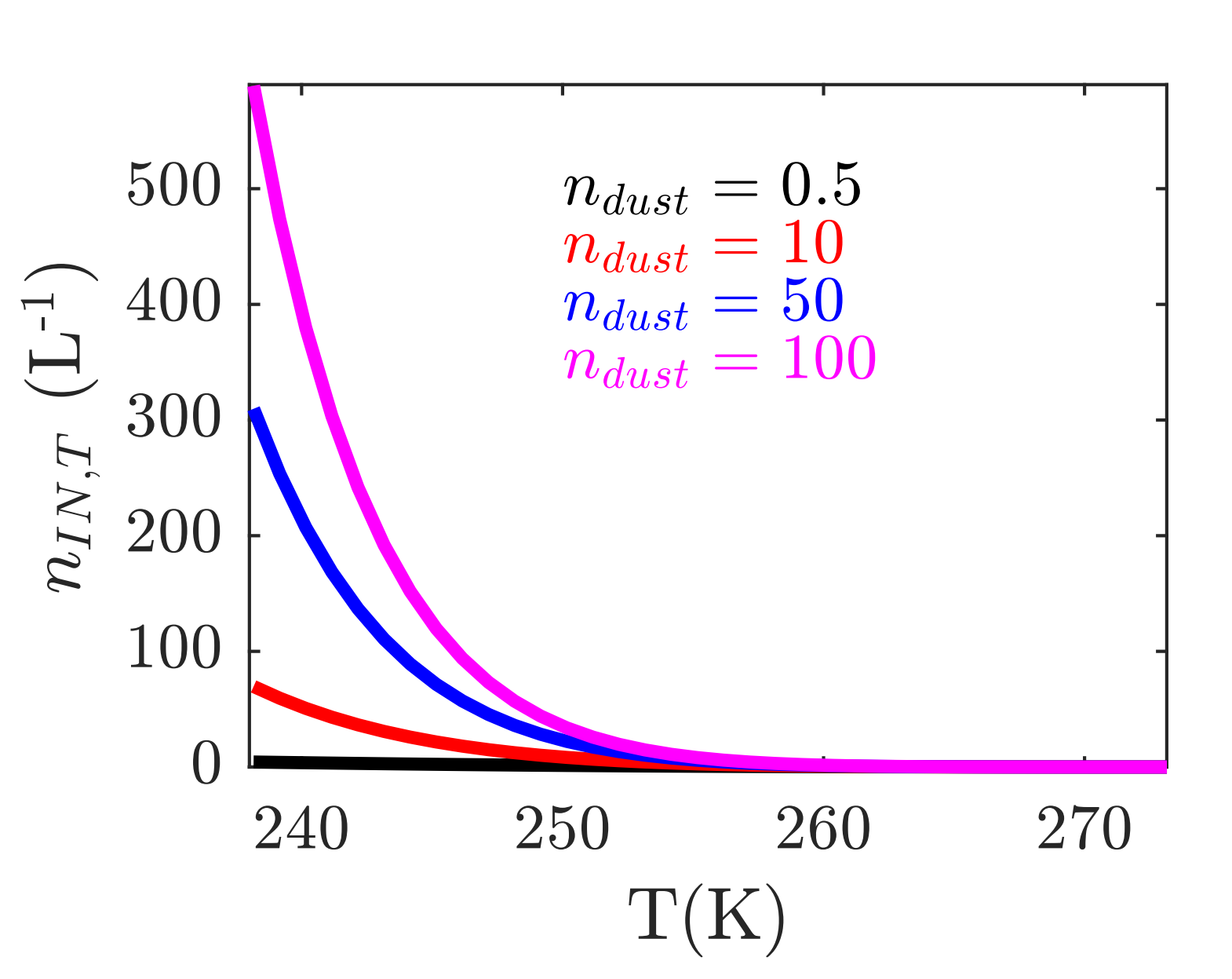
$n_{dust} = 0.5$
$n_{dust} = 10$
$n_{dust} = 50$
$n_{dust} = 100$
500
400
300
200
100
0
$n_{IN,T}$ (L^{-1})
240
250
260
270
T(K)

Figure 7.

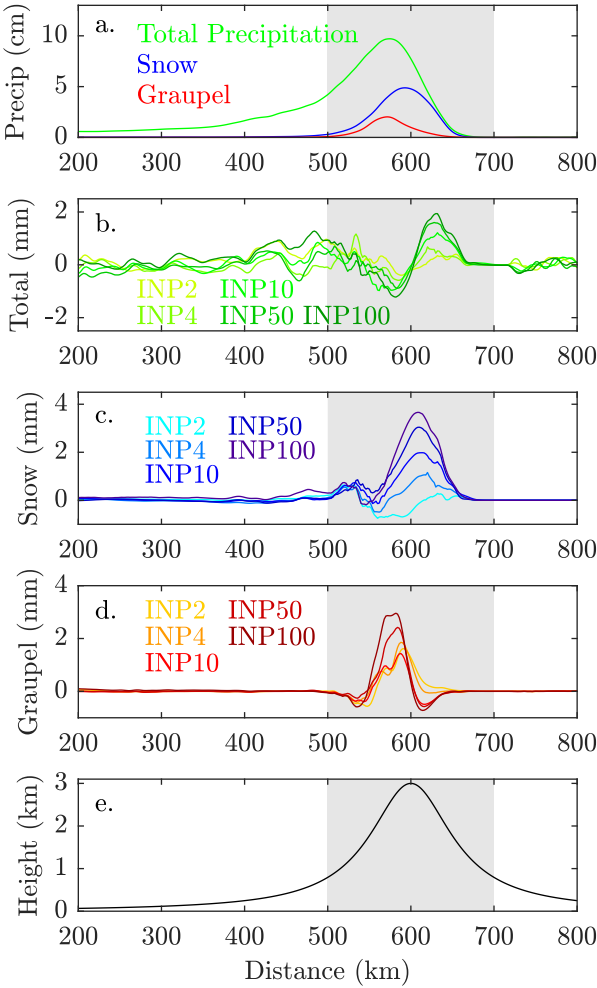
a.
Total Precipitation
Snow
Graupel
Precip (cm)
10
5
0
b.
Total (mm)
2
0
-2
INP2
INP10
INP4
INP50
INP100
c.
Snow (mm)
4
2
0
INP2
INP50
INP4
INP100
INP10
d.
Graupel (mm)
4
2
0
INP2
INP50
INP4
INP100
INP10
e.
Height (km)
3
2
1
0
200
300
400
500
600
700
800
Distance (km)

Figure 8.

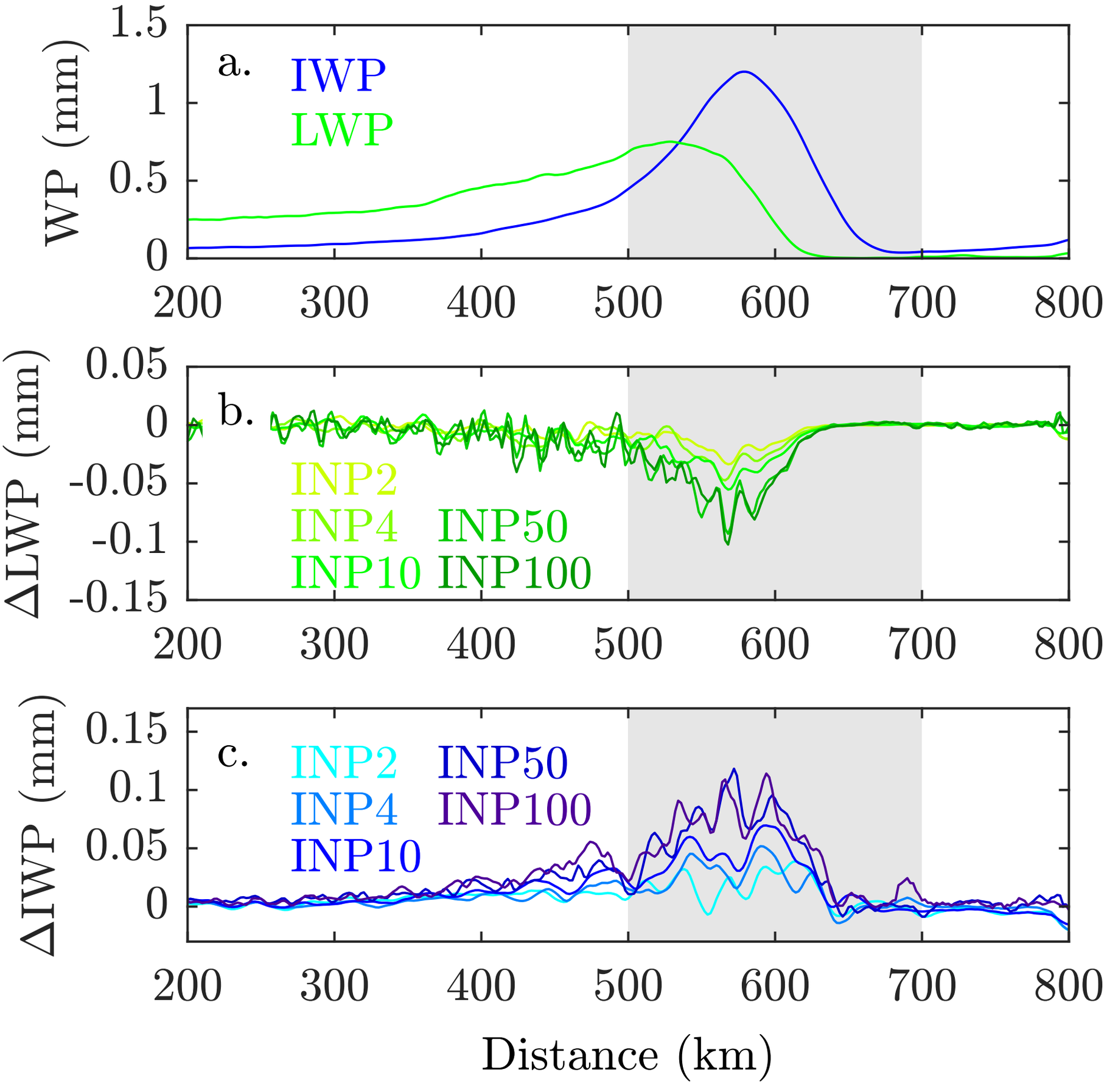
a.
IWP
LWP
WP (mm)
1.5
1
0.5
0
200
300
400
500
600
700
800
b.
INP2
INP4
INP50
INP10
INP100
ΔLWP (mm)
0.05
0
-0.05
-0.1
-0.15
c.
INP2
INP50
INP4
INP100
INP10
ΔIWP (mm)
0.15
0.1
0.05
Distance (km)

Figure 9.

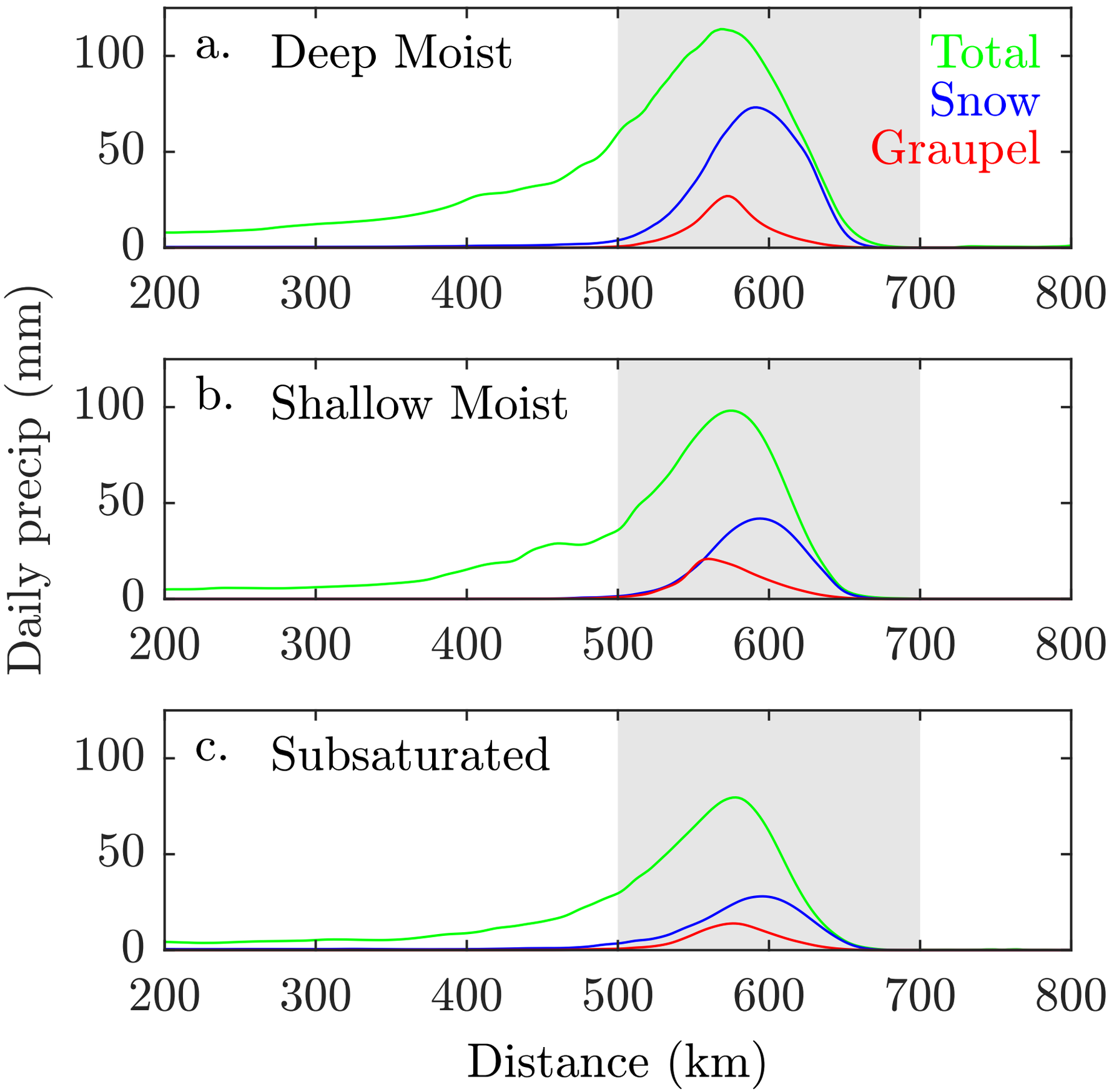
a. Deep Moist
b. Shallow Moist
c. Subsaturated
Total
Snow
Graupel
Daily precip (mm)
Distance (km)
0
50
100
200
300
400
500
600
700
800

Figure 10.

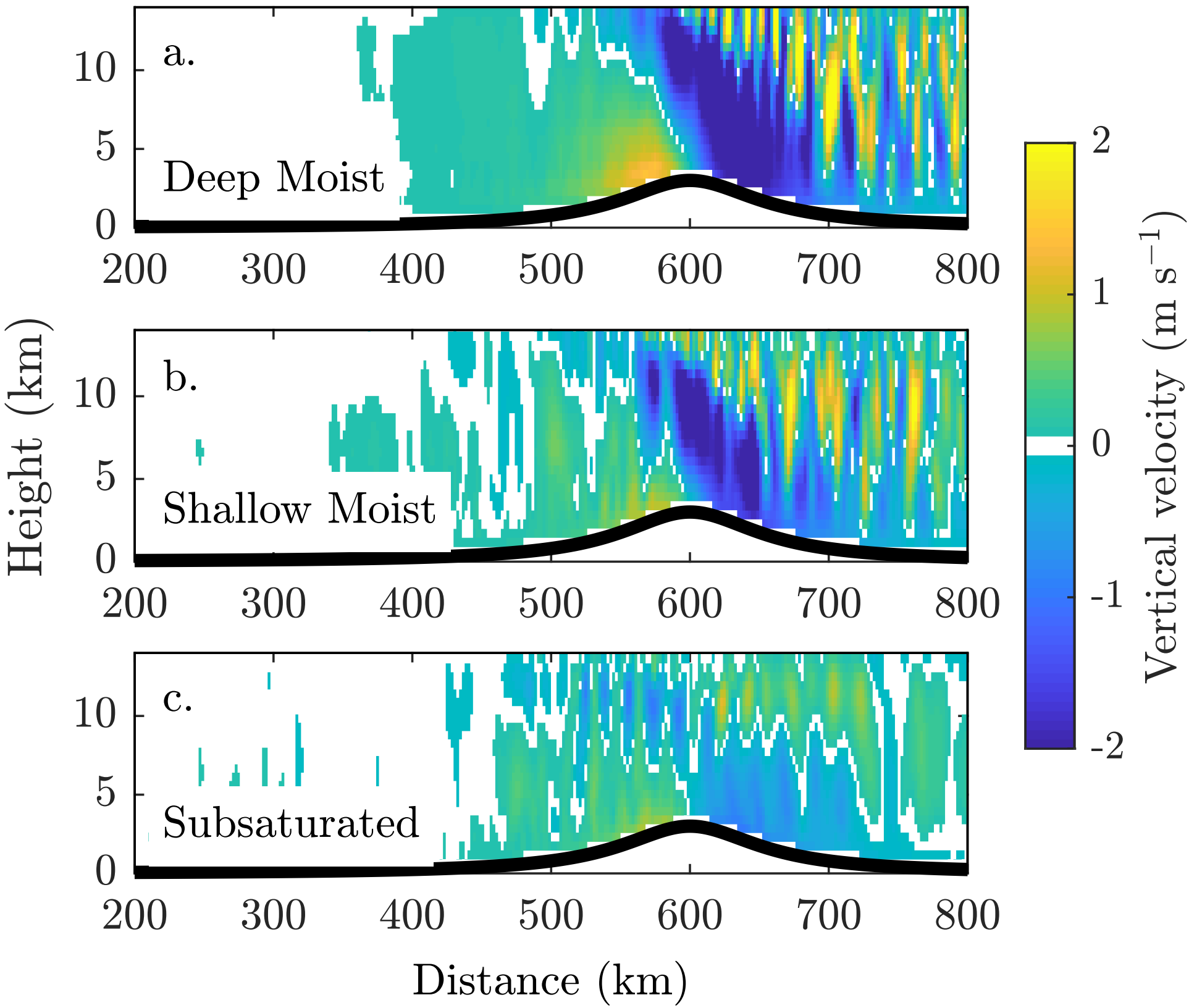
a.
Deep Moist
b.
Shallow Moist
c.
Subsaturated
10
5
0
200
300
400
500
600
700
800
Height (km)
Distance (km)
2
1
0
-1
-2
Vertical velocity (m s^{-1})

Figure 11.

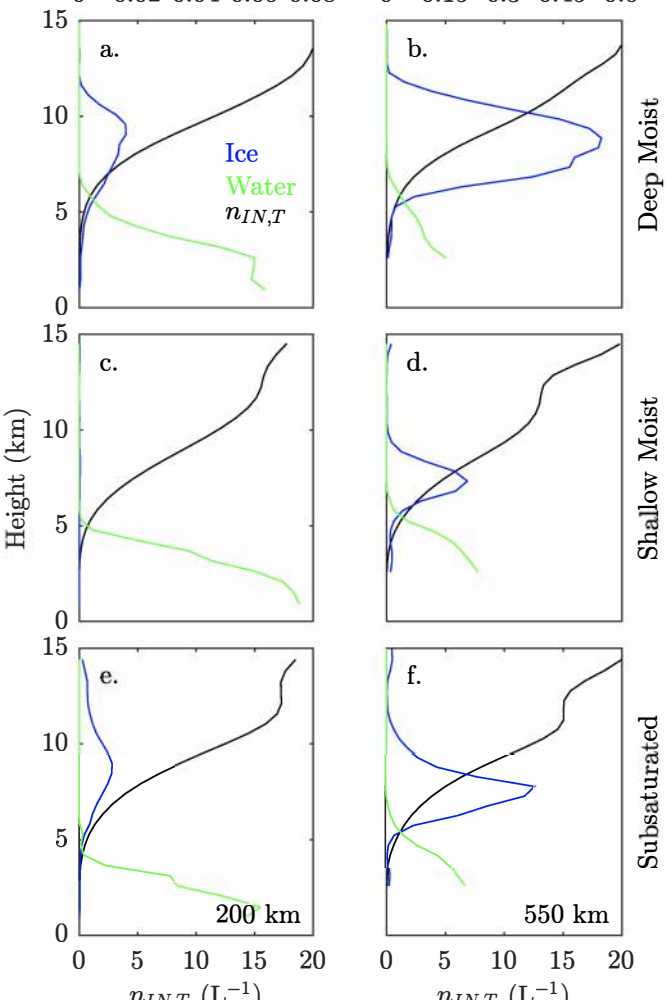
Mixing ratio (g kg^{-1})
0 0.02 0.04 0.06 0.08
Mixing ratio (g kg^{-1})
0 0.15 0.3 0.45 0.6
a.
b.
c.
d.
e.
f.
Ice
Water
$n_{IN,T}$
Deep Moist
Shallow Moist
Subsaturated
Height (km)
0 5 10 15
200 km
550 km
0 5 10 15 20
$n_{IN,T}$ (L^{-1})

Figure 12.

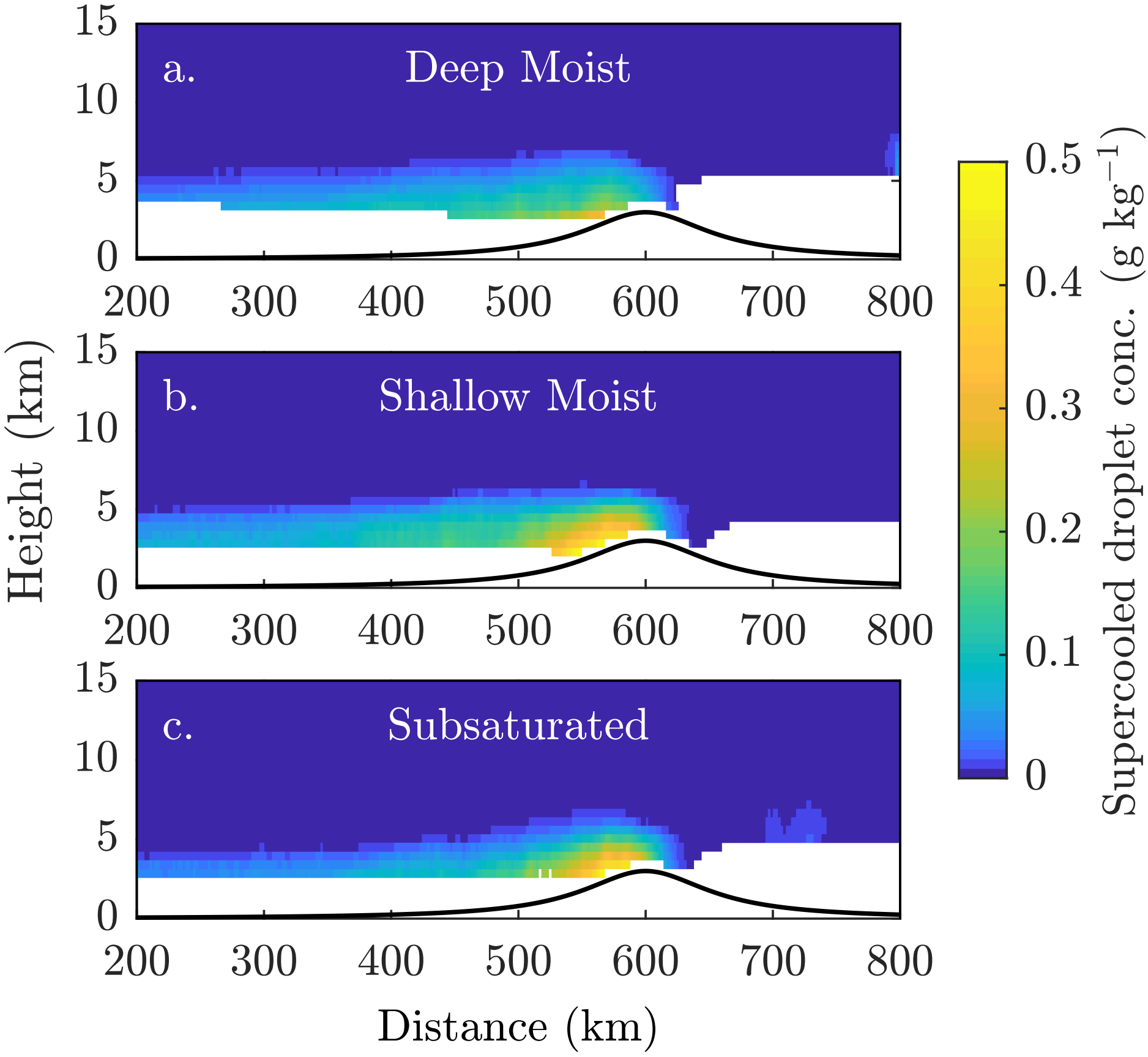
a.
Deep Moist
b.
Shallow Moist
c.
Subsaturated
15
10
5
0
200
300
400
500
600
700
800
Height (km)
Distance (km)
0.5
0.4
0.3
0.2
0.1
0
Supercooled droplet conc. (g kg^{-1})

Figure 13.

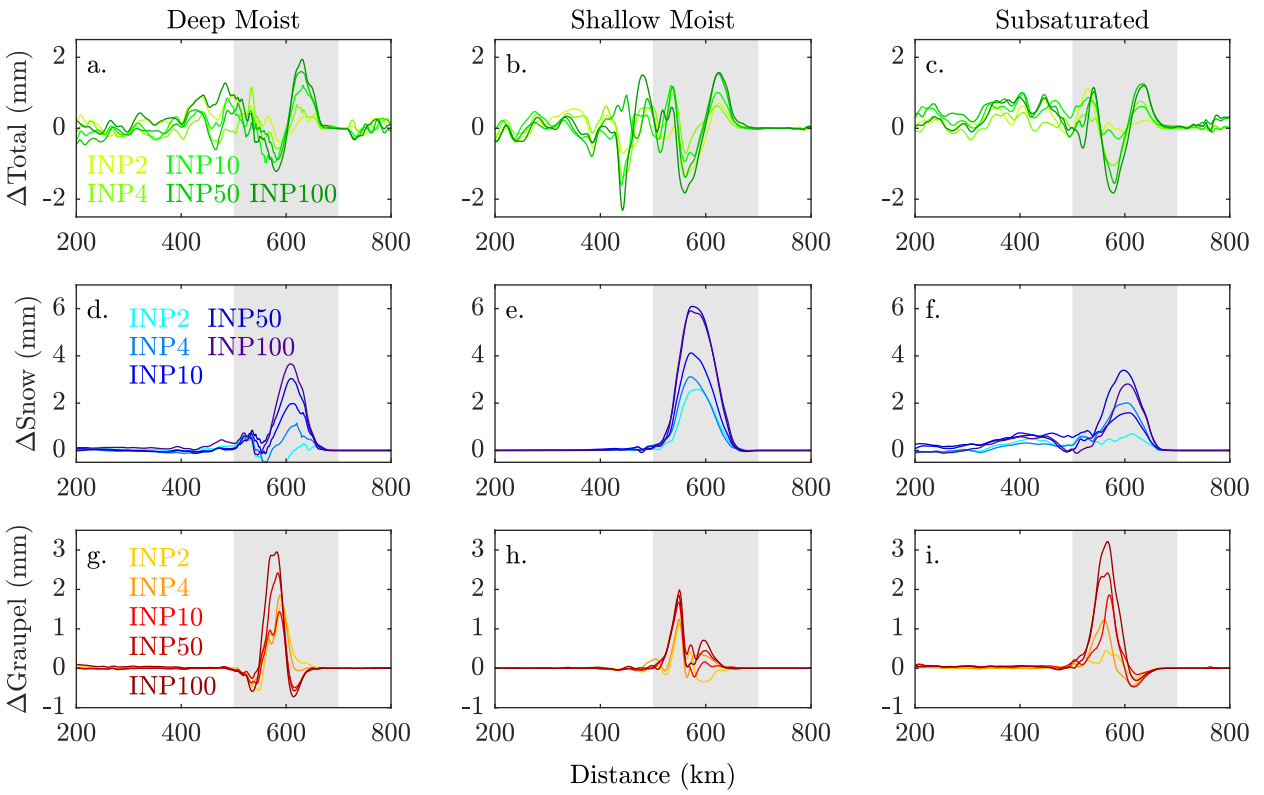
Deep Moist
Shallow Moist
Subsaturated
a.
b.
c.
d.
e.
f.
g.
h.
i.
ΔTotal (mm)
ΔSnow (mm)
ΔGraupel (mm)
INP2
INP10
INP4
INP50
INP100
Distance (km)

Figure 14.

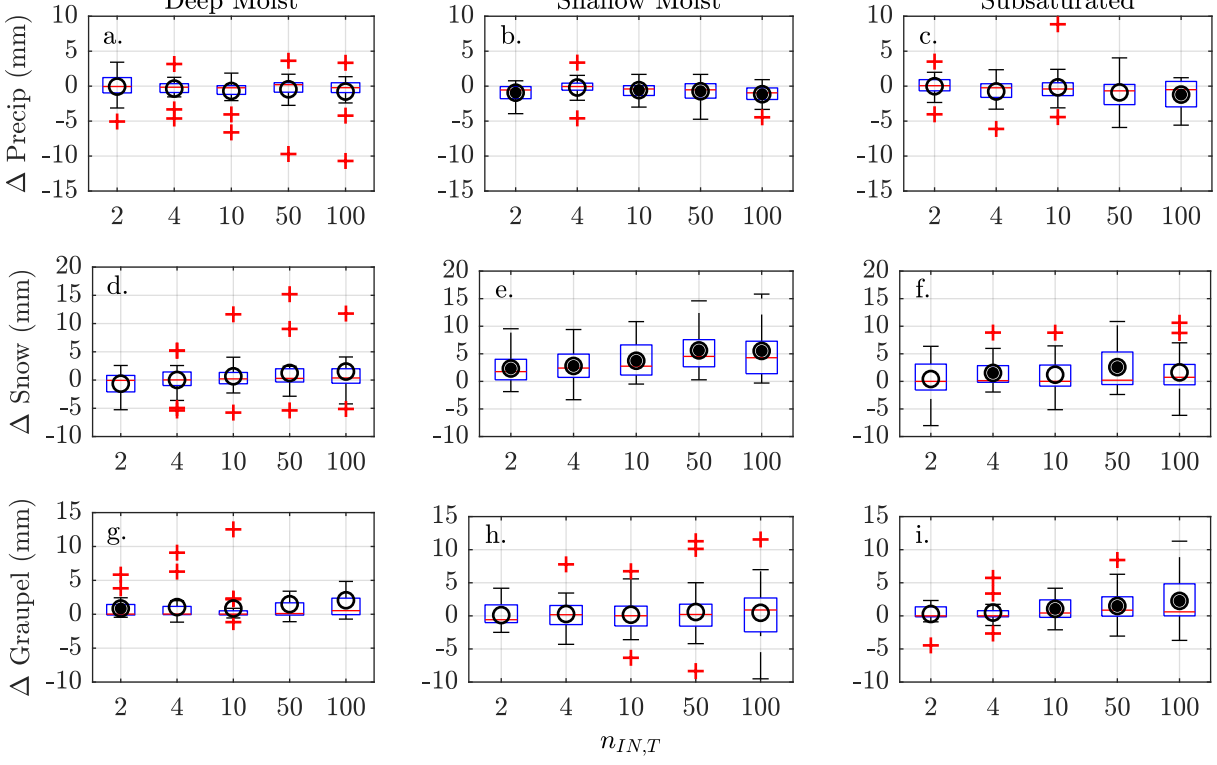
Deep Moist
Shallow Moist
Subsaturated
Δ Precip (mm)
Δ Snow (mm)
Δ Graupel (mm)
a.
b.
c.
d.
e.
f.
g.
h.
i.
$n_{IN,T}$

Figure 15.

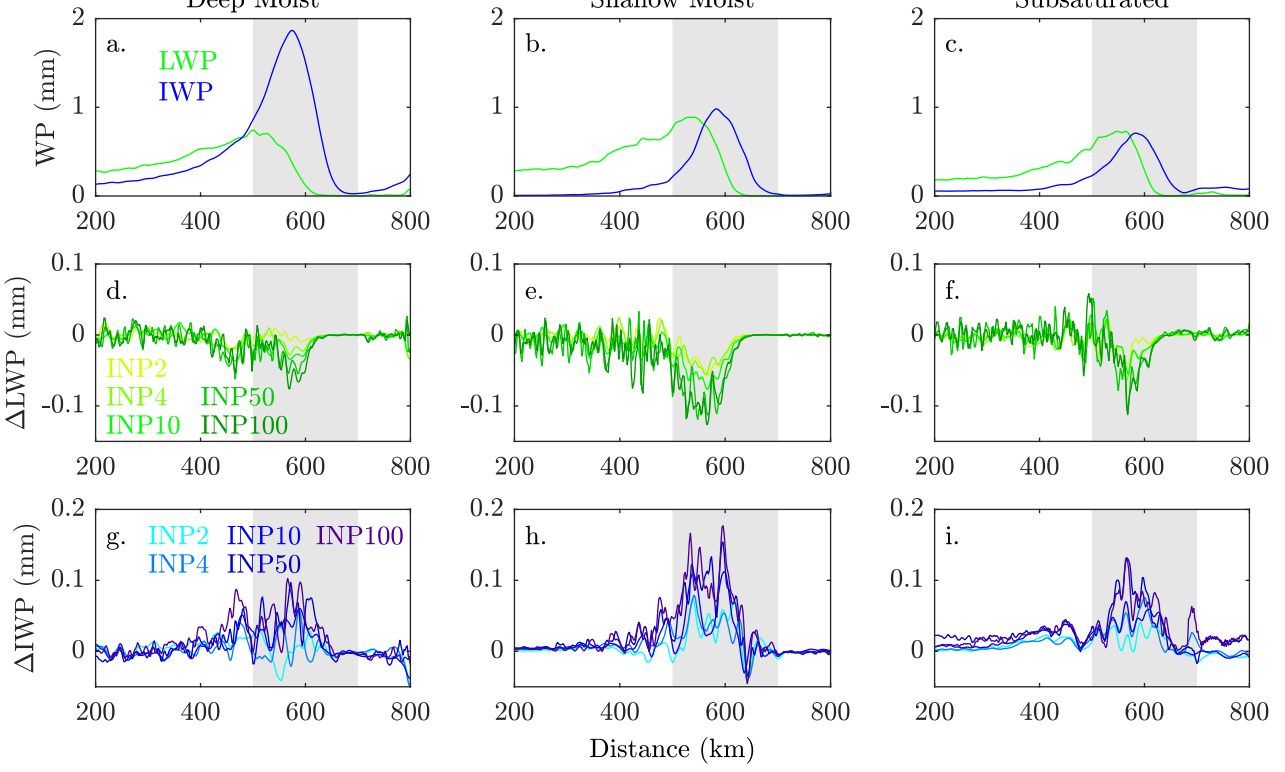
Deep Moist
Shallow Moist
Subsaturated
a.
b.
c.
LWP
IWP
WP (mm)
d.
e.
f.
INP2
INP4
INP10
INP50
INP100
ΔLWP (mm)
g.
h.
i.
INP2
INP4
INP10
INP50
INP100
ΔIWP (mm)
Distance (km)

Figure 16.

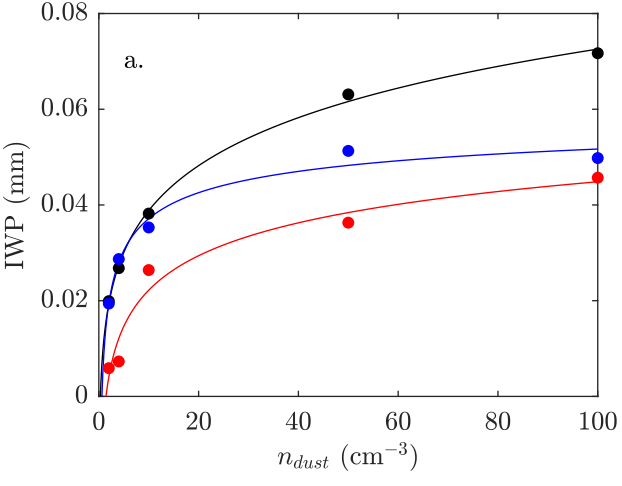
a.
IWP (mm)
0.08
0.06
0.04
0.02
0
0
20
40
60
80
100
n_{dust} (cm^{-3})

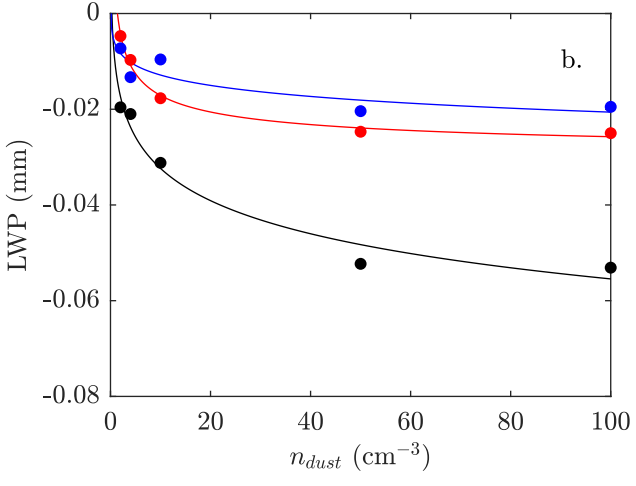
b.
LWP (mm)
0
-0.02
-0.04
-0.06
-0.08
0
20
40
60
80
100
n_{dust} (cm^{-3})

Figure 17.

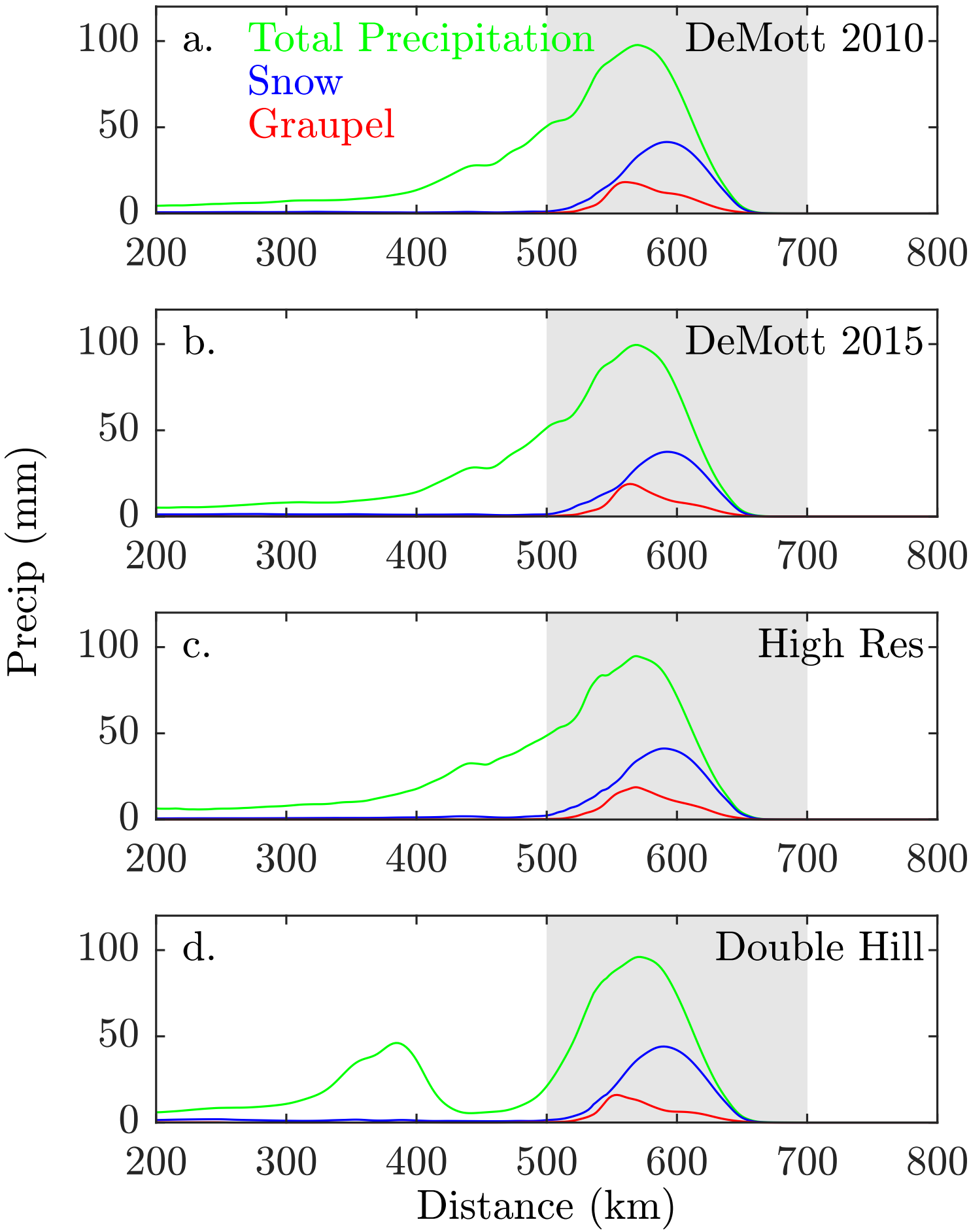
a.
Total Precipitation
Snow
Graupel
DeMott 2010
b.
DeMott 2015
c.
High Res
d.
Double Hill
Precip (mm)
Distance (km)
0
50
100
200
300
400
500
600
700
800

Figure 18.

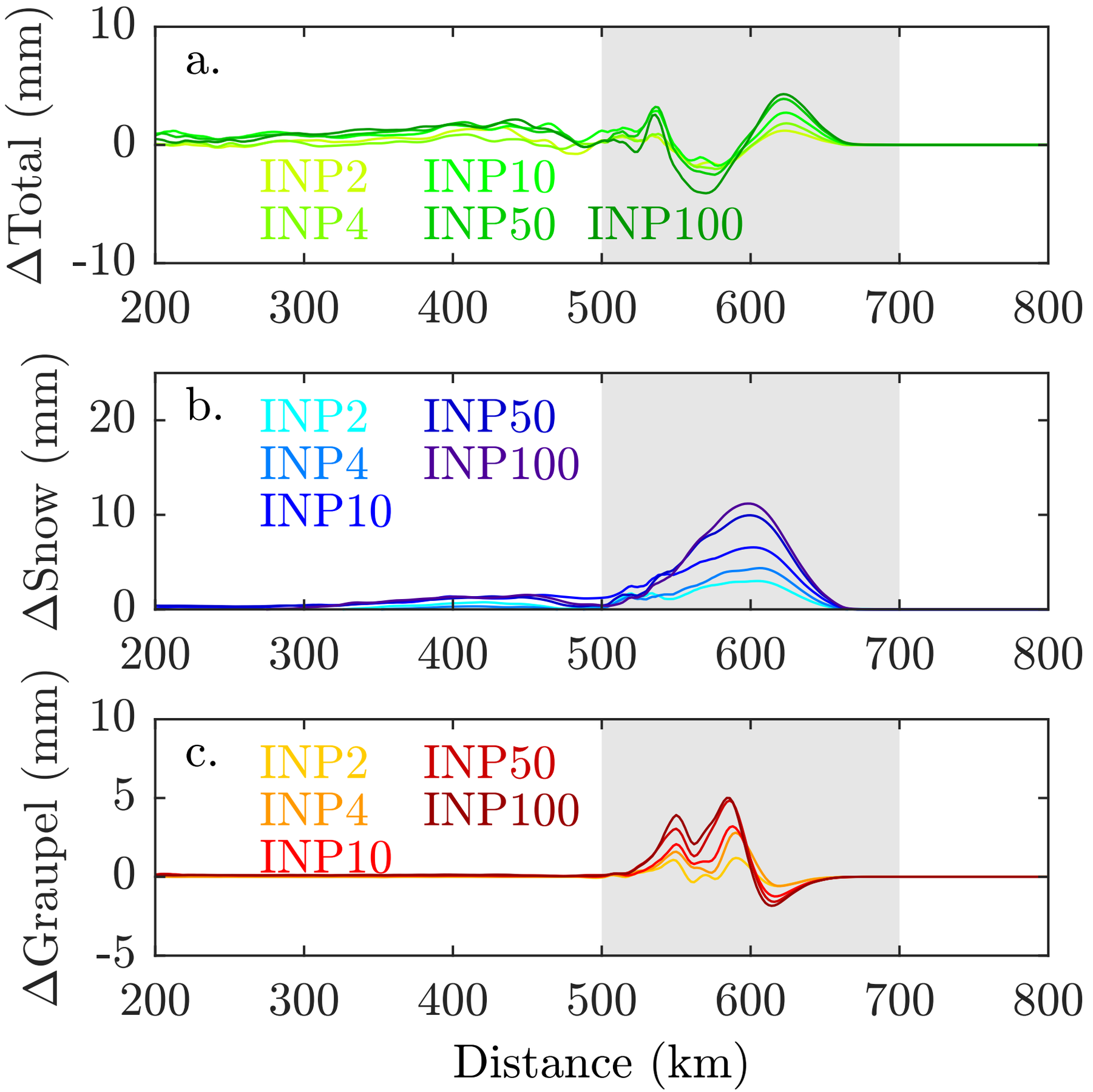
a.
INP2
INP4
INP10
INP50
INP100
ΔTotal (mm)
10
0
-10
200
300
400
500
600
700
800
b.
INP2
INP4
INP10
INP50
INP100
ΔSnow (mm)
20
10
0
c.
INP2
INP4
INP10
INP50
INP100
ΔGraupel (mm)
10
5
0
-5
Distance (km)

Figure 19.

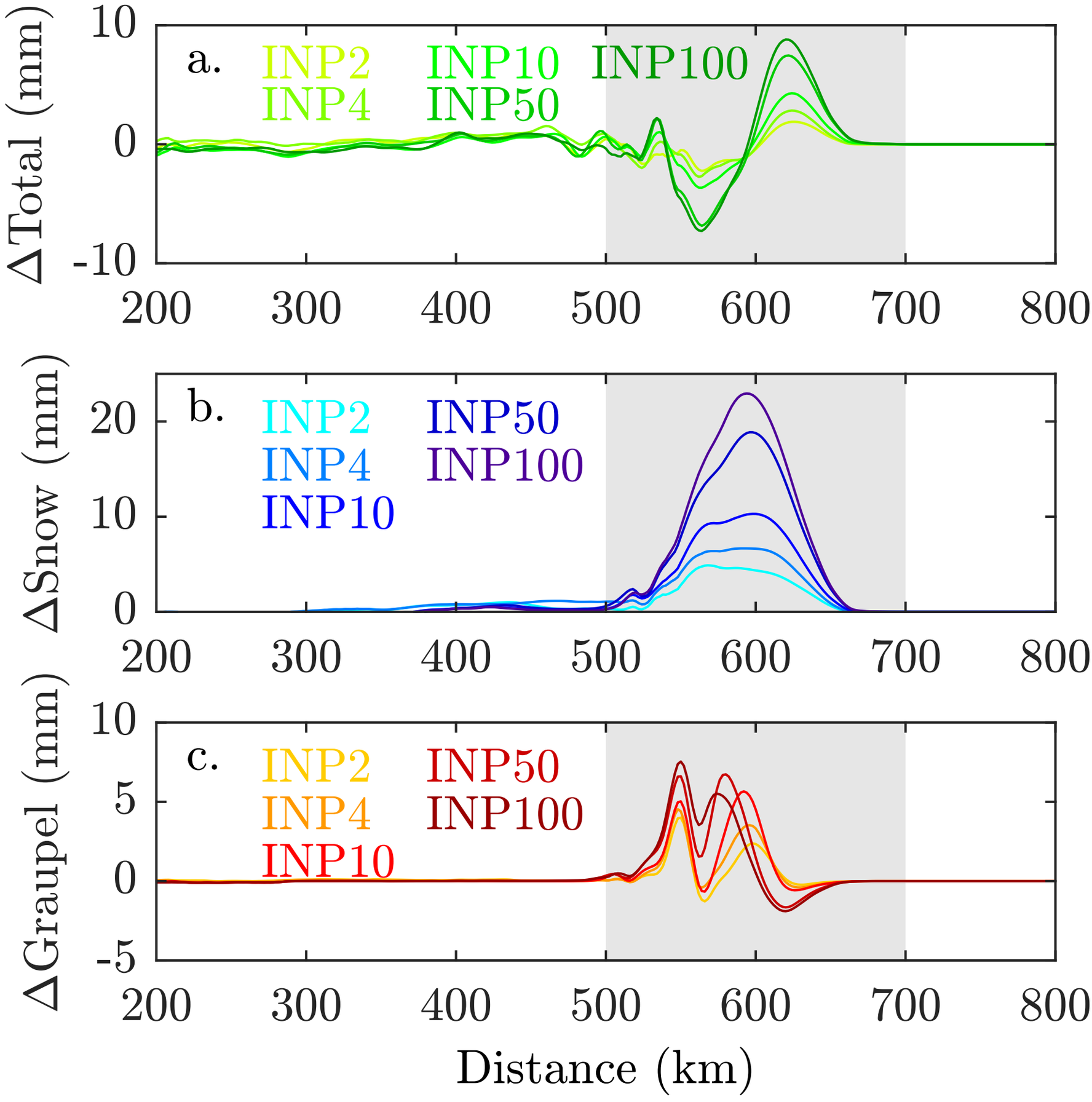
a.
INP2
INP4
INP10
INP50
INP100
ΔTotal (mm)
10
0
-10
200
300
400
500
600
700
800
b.
INP2
INP4
INP10
INP50
INP100
ΔSnow (mm)
20
10
0
c.
INP2
INP4
INP10
INP50
INP100
ΔGraupel (mm)
10
5
0
-5
Distance (km)

Figure 20.

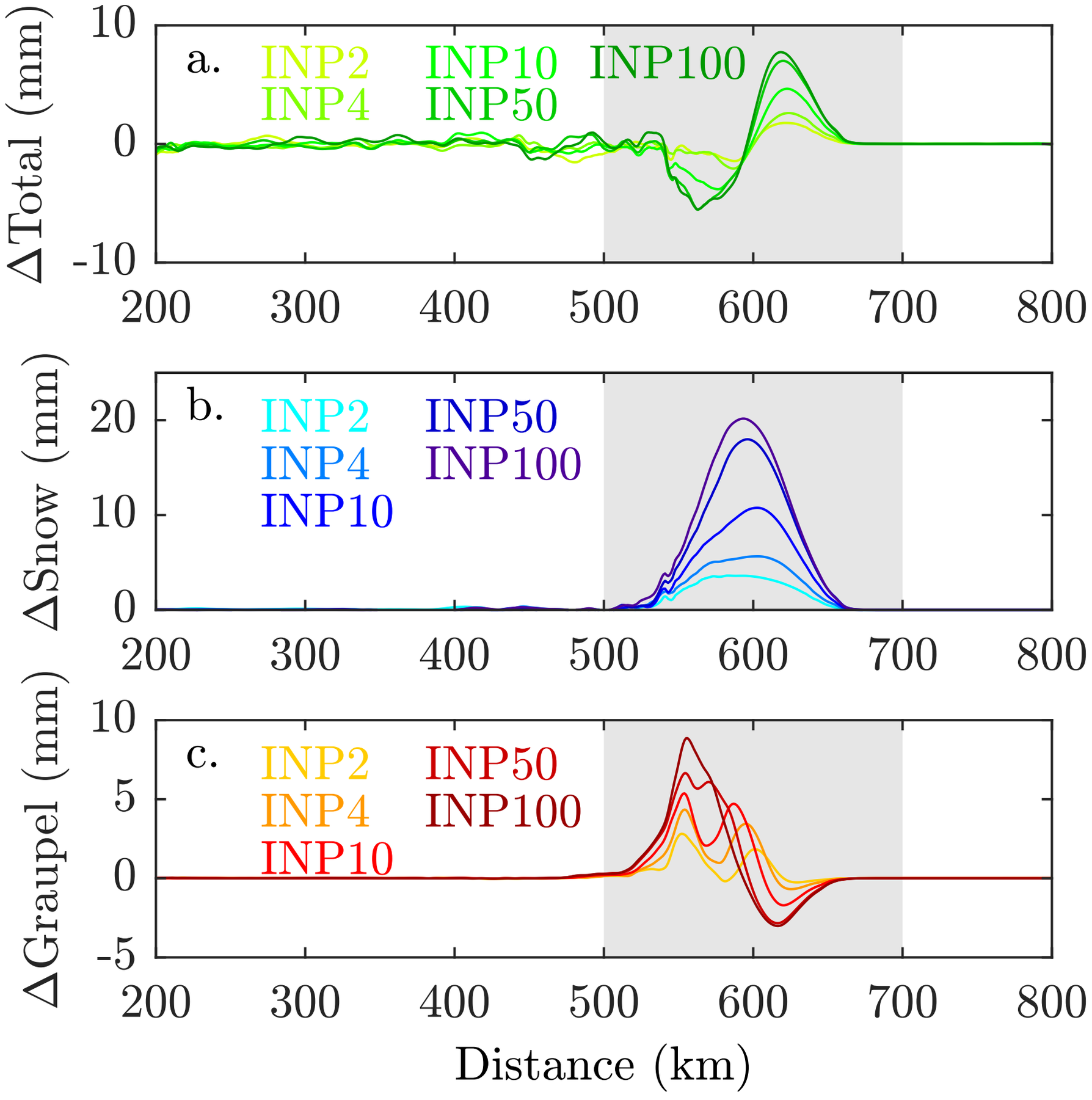
a.
INP2
INP4
INP10
INP50
INP100
ΔTotal (mm)
10
0
-10
200
300
400
500
600
700
800
b.
INP2
INP4
INP10
INP50
INP100
ΔSnow (mm)
20
10
0
c.
INP2
INP4
INP10
INP50
INP100
ΔGraupel (mm)
5
-5
Distance (km)

Figure 21.

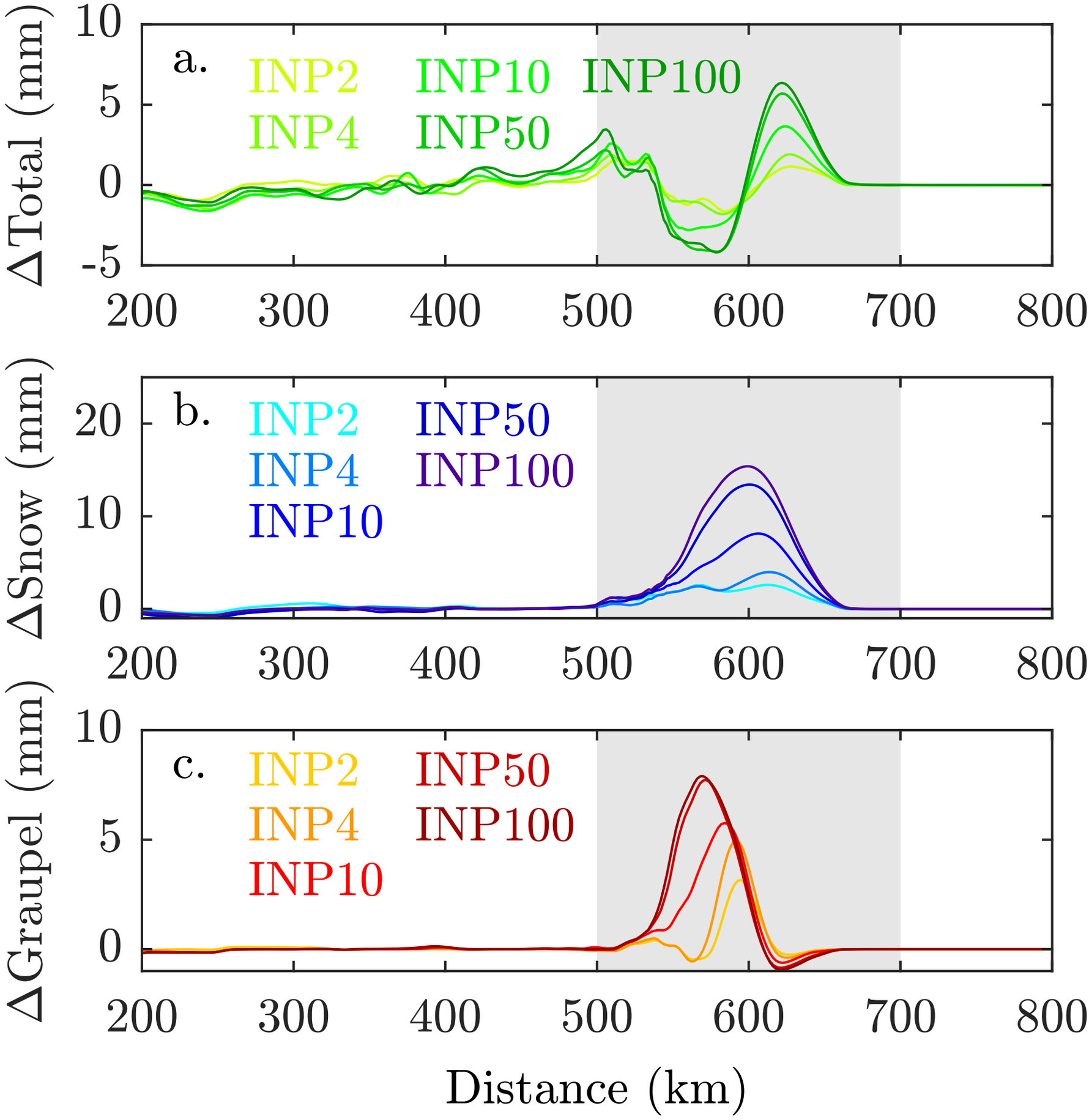
a.
INP2
INP4
INP10
INP50
INP100
ΔTotal (mm)
10
5
0
-5
b.
INP2
INP4
INP10
INP50
INP100
ΔSnow (mm)
20
10
0
c.
INP2
INP4
INP10
INP50
INP100
ΔGraupel (mm)
10
5
0
200
300
400
500
600
700
800
Distance (km)

Figure 22.

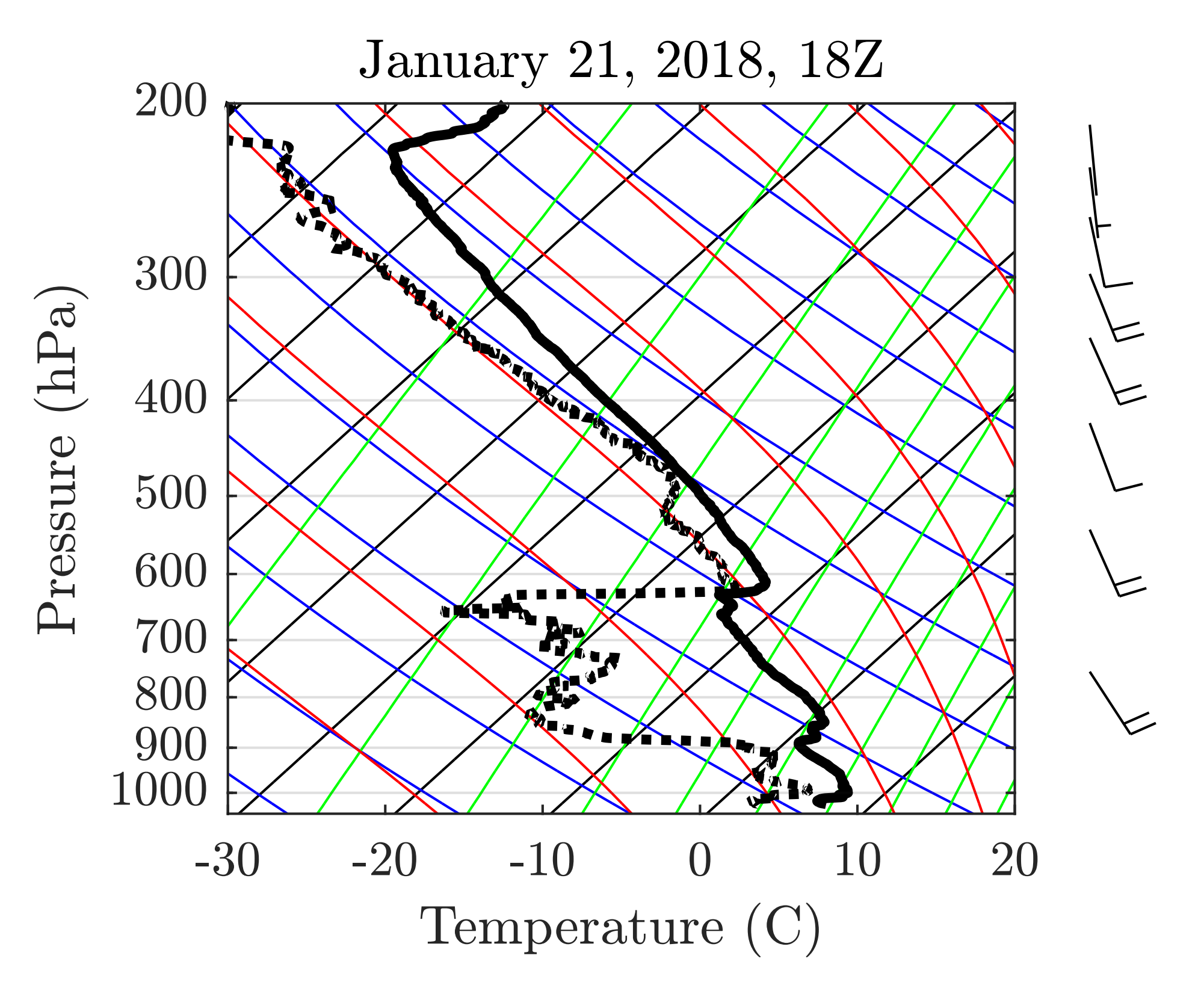
January 21, 2018, 18Z
Pressure (hPa)
200
300
400
500
600
700
800
900
1000
-30
-20
-10
0
10
20
Temperature (C)

Figure 23.

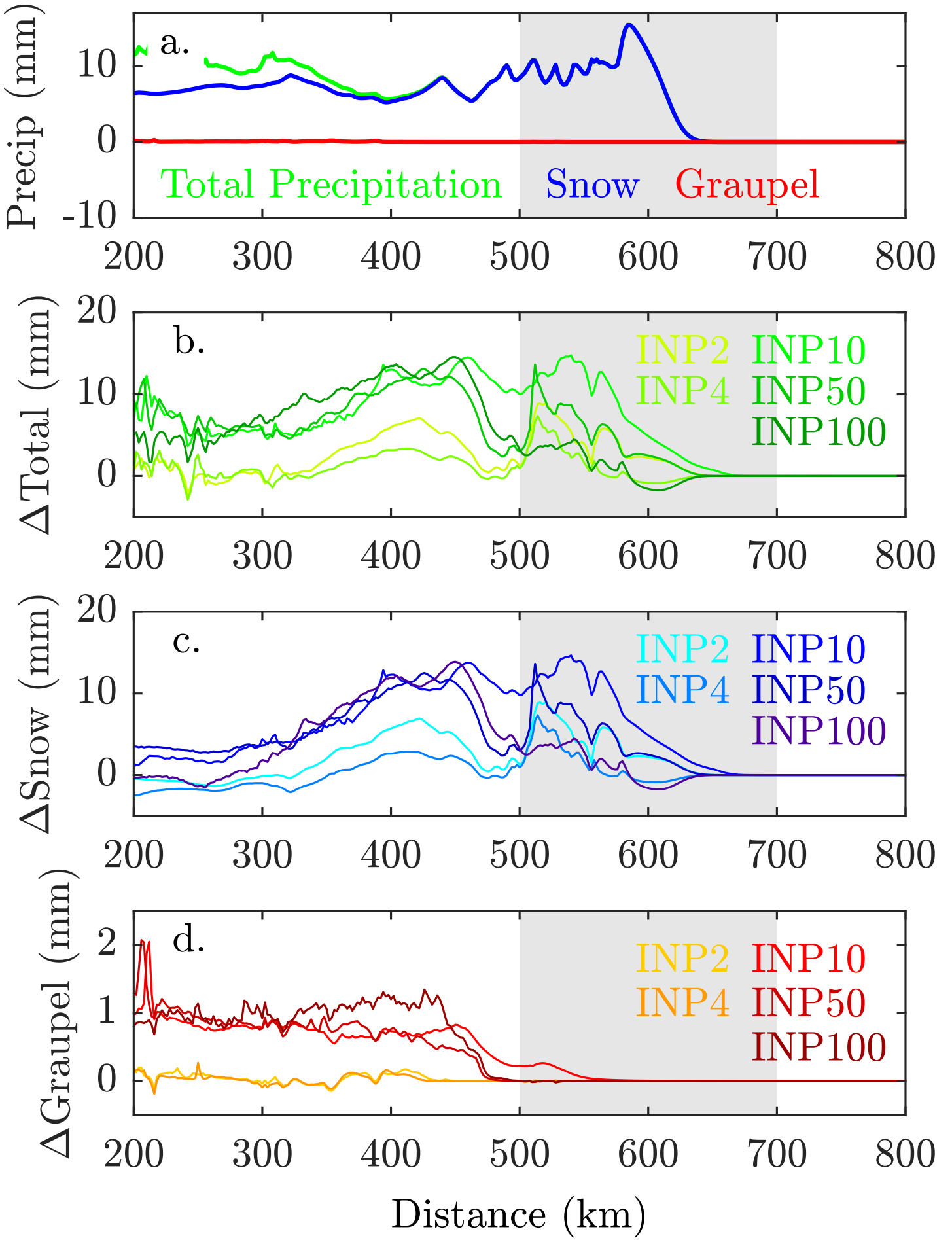
a.
Precip (mm)
10
0
-10
Total Precipitation
Snow
Graupel
200
300
400
500
600
700
800
b.
ΔTotal (mm)
20
10
0
INP2
INP4
INP10
INP50
INP100
c.
ΔSnow (mm)
d.
ΔGraupel (mm)
2
1
Distance (km)

Figure 24.

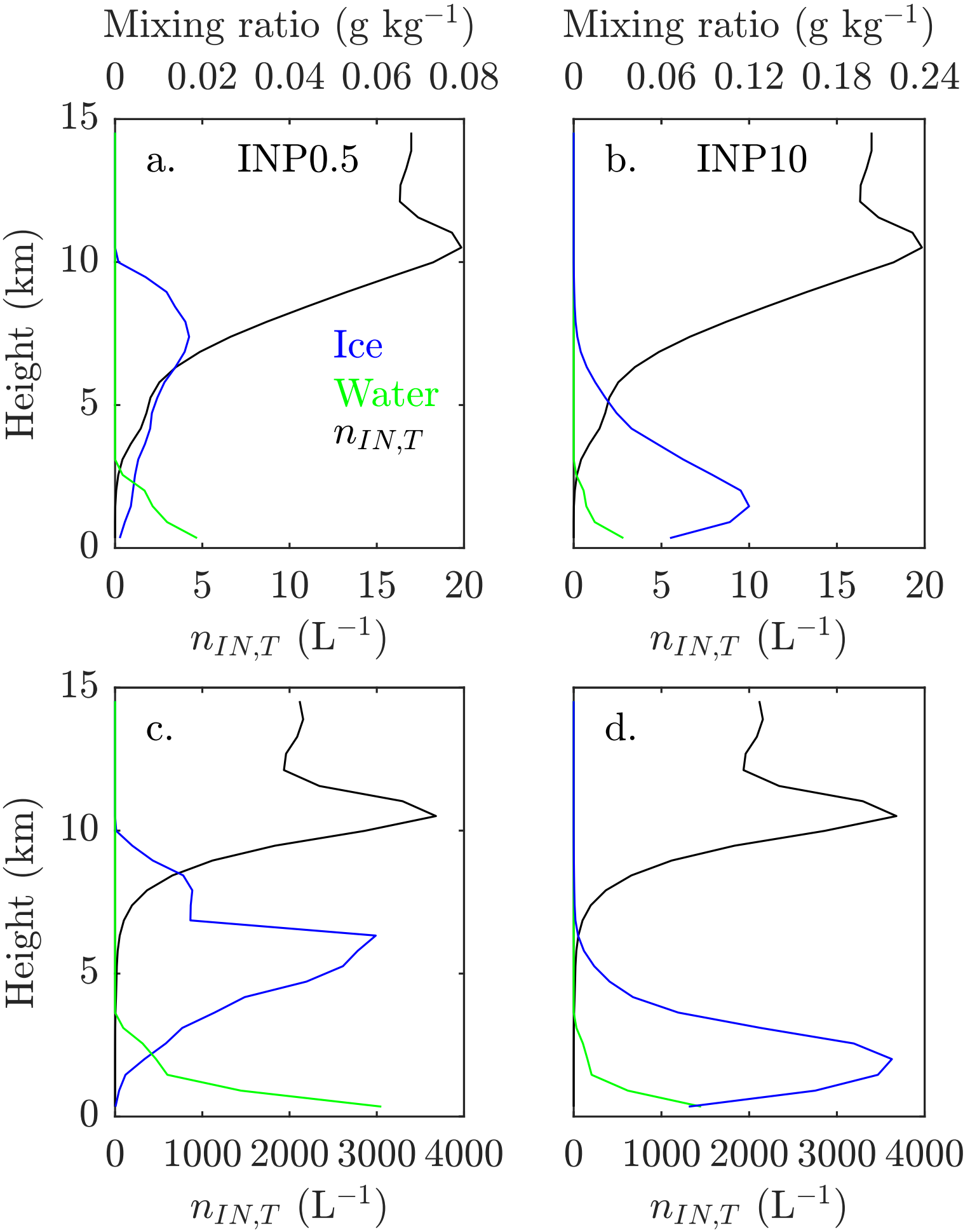
Mixing ratio (g kg^{-1})
0 0.02 0.04 0.06 0.08
Mixing ratio (g kg^{-1})
0 0.06 0.12 0.18 0.24
a. INP0.5
b. INP10
c.
d.
Ice
Water
$n_{IN,T}$
Height (km)
0 5 10 15
0 5 10 15 20
0 1000 2000 3000 4000
$n_{IN,T}$ (L^{-1})